## Title

Analysis of Cytochrome P450 CYP119 Ligand-dependent Conformational Dynamics by Two-dimensional NMR and X-ray Crystallography*



## Journal

Journal of Biological Chemistry, 290(16)

## ISSN

0021-9258

## Authors

Basudhar, Debashree
Madrona, Yarrow
Kandel, Sylvie
et al.

## Publication Date

2015-04-01

## DOI

10.1074/jbc.m114.627935

Peer reviewed

THE JOURNAL OF BIOLOGICAL CHEMISTRY VOL. 290, NO. 16, pp. 10000–10017, April 17, 2015


# Analysis of Cytochrome P450 CYP119 Ligand-dependent Conformational Dynamics by Two-dimensional NMR and X-ray Crystallography*

Received for publication, November 24, 2014, and in revised form, February 9, 2015 Published, JBC Papers in Press, February 10, 2015, DOI 10.1074/jbc.M114.627935

**Debashree Basudhar**[‡], **Yarrow Madrona**[‡], **Sylvie Kandel**[§], **Jed N. Lampe**[¶], **Clinton R. Nishida**[‡], **and Paul R. Ortiz de Montellano**[‡1]

*From the* [‡]*Department of Pharmaceutical Chemistry, University of California at San Francisco, San Francisco, California 94158,* [§]*XenoTech, LLC, Lenexa, Kansas 66219, and the* [¶]*Department of Pharmacology, Toxicology and Therapeutics, University of Kansas Medical Center, Kansas City, Kansas 66160*

**Background:** CYP119 structural rearrangements were examined by $^{1}H,^{15}N$ HSQC NMR of $^{15}N$-labeled Phe residues and x-ray crystallography.
**Results:** In solution, an open conformation of CYP119 is favored, but ligand-dependent F-G loop rearrangements produce two distinct closed conformations.
**Conclusion:** The two closed conformations are generated by ligands that differ by a fluoro to chloro substitution.
**Significance:** Cytochrome P450 enzymes ratchet among a discontinuous set of discrete conformations.

**Defining the conformational states of cytochrome P450 active sites is critical for the design of agents that minimize drug-drug interactions, the development of isoform-specific P450 inhibitors, and the engineering of novel oxidative catalysts. We used two-dimensional $^{1}H,^{15}N$ HSQC chemical shift perturbation mapping of $^{15}N$-labeled Phe residues and x-ray crystallography to examine the ligand-dependent conformational dynamics of CYP119. Active site Phe residues were most affected by the binding of azole inhibitors and fatty acid substrates, in agreement with active site localization of the conformational changes. This was supported by crystallography, which revealed movement of the F-G loop with various azoles. Nevertheless, the NMR chemical shift perturbations caused by azoles and substrates were distinguishable. The absence of significant chemical shift perturbations with several azoles revealed binding of ligands to an open conformation similar to that of the ligand-free state. In contrast, 4-phenylimidazole caused pronounced NMR changes involving Phe-87, Phe-144, and Phe-153 that support the closed conformation found in the crystal structure. The same closed conformation is observed by NMR and crystallography with a *para*-fluoro substituent on the 4-phenylimidazole, but a *para*-chloro or bromo substituent engendered a second closed conformation. An open conformation is thus favored in solution with many azole ligands, but *para*-substituted phenylimidazoles give rise to two closed conformations that depend on the size of the *para*-substituent. The results suggest that ligands selectively stabilize discrete cytochrome P450 conformational states.**

The conformational flexibility of cytochrome P450 enzymes is important for their ability to recognize and to regio- and stereoselectively oxidize a diverse range of endogenous and exogenous molecules (1–3). An understanding of the conformational determinants of cytochrome P450 ligand binding is essential for several reasons. First, cytochrome P450 enzymes are responsible for the bulk of the oxidative metabolism of drugs and xenobiotics, and managing this oxidative metabolism has become a critical aspect of the design of new pharmaceutical agents. Cytochrome P450 enzymes are also, in themselves, potential drug targets, as it is estimated that they account for more than 2% of the druggable targets in the human genome (4). Furthermore, cytochrome P450 enzymes have promising biotechnological applications, including in the synthesis of complex organic molecules and the removal of environmental pollutants (5, 6).

The most general and effective pharmacophore for the design of cytochrome P450 inhibitors is the azole moiety (7–9). Anastrozole and letrozole, two highly effective azole inhibitors that target CYP19A1 (aromatase), have recently been recommended as the first line chemotherapy for estrogen-dependent breast cancer (10, 11). Additionally, azole antifungal agents have been used successfully for decades to treat fungal diseases (12, 13). However, targeting a particular P450 enzyme selectively, while avoiding off-target effects on other host P450 enzymes, is both difficult and challenging, as many of the currently marketed azole antifungal agents are also potent inhibitors of oxidative liver drug metabolism (14).

The crystal structures of bacterial cytochrome 450 enzymes and of the heme domains of mammalian enzymes are now available both in the presence and absence of diverse ligands (15–18). These structures have provided highly useful information on the binding constraints for individual substrates and inhibitors. However, they do not necessarily report the range of accessible conformational states in solution, but rather they select the single most energetically stable conformation under a given set of crystallization conditions. As the conformational states in solution are the most biologically relevant, it is highly

* This work was supported, in whole or in part, by National Institutes of Health Grant GM25515.
*The atomic coordinates and structure factors (codes 4WPD, 4TUV, 4TT5, and 4WQJ) have been deposited in the Protein Data Bank (http://wwpdb.org/).*
[1] To whom correspondence should be addressed: Dept. of Pharmaceutical Chemistry, University of California at San Francisco, 600 16th St., San Francisco, CA 94158-2517. Tel.: 415-475-2903; E-mail: Ortiz@cgl.ucsf.edu.

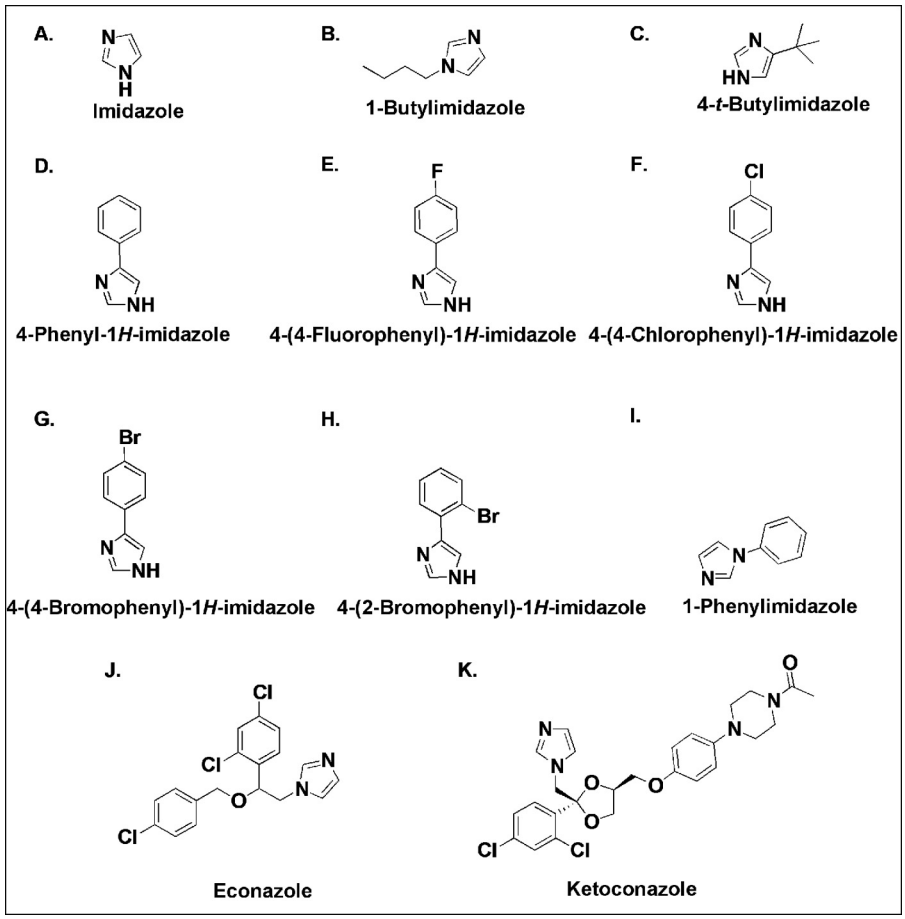


FIGURE 1. **Structures of azole inhibitors examined in this study: imidazole (*A*), 1-butylimidazole (*B*), 4-*t*-butylimidazole (*C*), 4-PI (*D*), 4-FPI (*E*), 4-CPI (*F*), 4-BPI (*G*), 2-BPI (*H*), 1-PI (*I*), econazole (*J*), and ketoconazole (*K*).**

desirable to complement the crystallographic structures with data from spectroscopic methods that provide independent information on the conformation of the enzymes in solution. NMR is one of the most powerful methodologies available for this purpose, as it provides an overview of the dynamic nature of the ligand binding process based on the movement of residues involved in protein-ligand interactions under physiologically relevant conditions. Furthermore, although crystal structures are limited to low energy conformations, NMR can also reveal the presence of additional higher energy states (19, 20).

Ligand binding to mammalian P450s is difficult to investigate by NMR due to their high molecular mass and propensity to aggregate. However, the relationships between ligand binding and protein conformation can be examined using the more soluble bacterial cytochrome P450 enzymes. Thus, the binding of ligands to CYP101 ($P450_{CAM}$), probably the most studied P450 enzyme, has been investigated by both one- and two-dimensional NMR spectroscopy (21–23) as well as crystallography (24–29). Solid state NMR has also been used recently to characterize the binding of cytochrome $b_5$ to mammalian membrane-bound P450 proteins (30–33). In this study, we focus on CYP119, a thermophilic cytochrome P450 enzyme from *Sulfolobus acidocaldarius,* because of its inherent stability, a conformational range akin to that of the mammalian P450 enzymes, and its suitability for NMR studies (34, 35). Previously, we investigated ligand-induced conformational changes in the F-G region of CYP119 by $^{1}H,^{13}C$ HSQC NMR after incorporating $^{13}C$-labeled 4-methoxyphenylalanine at the Phe-144, Phe-153, or Phe-162 positions (34, 35). The labeled proteins were studied with a low affinity inhibitor (imidazole), a high affinity inhibitor (4-phenylimidazole, 4-PI),[2] and a high affinity substrate (lauric acid). Although this method successfully distinguished the inhibitors from the substrate, it gave similar NMR spectra for both weak and tight binding inhibitors despite the major differences seen in the corresponding crystal structures. Also, NMR resonances associated with the ligand-free enzyme persisted even in the presence of excess ligand. These findings, coupled with molecular dynamics simulations, suggest that CYP119 samples a range of pre-determined conformational states in which ligand binding favors one conformation over the others (34). In this study, $^{15}N$-labeled Phe residues were used as *in situ* probes due to their buried nature and proximity to the active site to examine the protein structural rearrangements that occur on binding of a range of azole ligands of different size, shape, and lipophilicity (Fig. 1), as well as the binding of three substrates, using two-dimensional $^{1}H,^{15}N$

[2] The abbreviations used are: 4-PI, 4-phenylimidazole; 4-FPI, 4-(4-fluorophenyl)-1*H*-imidazole, 4-CPI, 4-(4-chlorophenyl)-1*H*-imidazole; 4-BPI, 4-(4-bromophenyl)-1*H*-imidazole; 1-PI, 1-phenylimidazole; BisTris, 2-[bis(2-hydroxyethyl)amino]-2-(hydroxymethyl)propane-1,3-diol; PDB, Protein Data Bank; 2-BPI, 4-(2-bromophenyl)-1*H*-imidazole.

HSQC NMR chemical shift perturbation of $^{15}$N-labeled Phe residues. $^{15}$N-Labeled Phe residues have been used previously to examine ligand binding cooperativity in cytochrome $P450_{eryF}$ (36). The purpose of this study was 2-fold. First, we wanted to further test the hypothesis concerning discrete conformational states, and second, to establish whether NMR could be used as a predictive tool to examine the binding mode of different sized ligands in CYP119, and by extension in mammalian P450 enzymes as well. As part of this effort, the x-ray crystal structures of CYP119 bound to 4-(4-fluorophenyl)-1*H*-imidazole (4-FPI), 4-(4-chlorophenyl)-1*H*-imidazole (4-CPI), or 4-(4-bromophenyl)-1*H*-imidazole (4-BPI) were also determined.

## MATERIALS AND METHODS

*Chemicals*—Unless otherwise noted, all chemicals and solvents used were of analytical grade and were obtained from Sigma. Water used was deionized and distilled in a Milli-Q apparatus. All the supplements were prepared using Millipore water that was filter-sterilized using a 0.22-$\mu$m filter.

*Construction of CYP119 Expression Vector for Different Phe Mutants*—The expression vectors used for the expression of C-terminal $His_6$-tagged Phe CYP119 mutants were constructed by amplification of the mutated CYP119 gene coding sequence from an existing pCW/*cyp119-CHis*$_6$ vector containing engineered BamHI and XbaI restriction cloning sites (37). As per the instructions of the QuikChange Lightning site-directed mutagenesis kit (Agilent), 2 $\mu$l of DpnI restriction enzyme was added to digest the parental supercoiled dsDNA and transformed in XL-10 ultracompetent cells. The resulting plasmid was purified and digested using XbaI and BamHI (New England Biolabs), and ligated into a similarly digested *pCWori*$^+$ vector to provide the expression vector *pCW*/mutant-*CYP119*-C$His_6$. The resulting plasmid was transformed into *Escherichia coli* DH5$\alpha$ cells for ampicillin screening, and the resulting construct was verified by sequencing. The following mutants were prepared: F5L, F24L, F36L, F39L, F60L, F87L, F98L, F144L, F153L, F162Y, F225L, F228L, F292L, F298L, F310Y, F334L, and F338Y.

*Expression of $^{15}$N-Phe-CYP119 and Its Mutants*—The *pCWori*$^+$ vector containing the CYP119/mutant gene encoding a $His_6$ tag at the C terminus was transformed into the DH-5$\alpha$ strain of *E. coli* (Invitrogen) and plated on agar plate containing 100 mg/ml ampicillin. The resulting plate was incubated at 37 °C for 18 h. Following transformation, a single *E. coli* colony was used to inoculate a 50-ml culture of Luria-Bertani (LB) broth containing 100 $\mu$g/ml ampicillin, which was then incubated overnight at 37 °C at 250 rpm. A 10-ml aliquot of this starter culture was then used to inoculate 1 liter of autoclaved minimal expression medium containing a mixture of $K_2HPO_4$ (10 g/liter, 57.4 mM), sodium acetate (1.0 g/liter, 7.4 mM), $NH_4Cl$ (2.0 g/liter, 37.4 mM), sodium succinate (2.75 g/liter, 10.2 mM), glycerol (0.8% v/v), and the following amino acids: Cys, Ser, Ala, Gln, Glu, Arg, and Gly (400 mg/liter each); Asp and Met (250 mg/liter each); His, Ile, Leu, Lys, Asn, Pro, Thr, Val, Trp, and Tyr (100 mg/liter each); the following nucleosides: cytosine and thiamine (200 mg/liter each); uracil and adenine (400 mg/liter each); guanosine (500 mg/liter). The medium was also supplemented with the sterile filtered stock solutions of $Mg(OAc)_2$ (0.96 g/liter, 4.5 mM), $CaCl_2$ (14.7 mg/liter, 6.8 mM), biotin (0.5 mg/liter, 2.05 $\mu$M), nicotinamide (100 mg/liter, 0.82 mM), thymine (50 mg/liter, 1.6 mM), ampicillin (100 mg/liter), and a trace element solution (0.25 ml), containing $FeCl_3 \cdot 6H_2O$ (2.7 g/100 ml, 99.1 mM), $ZnCl_2 \cdot 4H_2O$ (0.2 g/100 ml, 9.6 mM), $CoCl_2 \cdot 6H_2O$ (0.2 g/100 ml, 8.4 mM), $CaCl_2 \cdot 2H_2O$ (0.1 g/100 ml, 6.8 mM), $Na_2MoO_4 \cdot 2H_2O$ (0.2 g/100 ml, 8.3 mM), $CuCl_2$ (0.1 g/100 ml, 7.4 mM), $H_3BO_3$ (0.05 g/100 ml, 8.1 mM), and 10 ml of concentrated HCl. $^{15}$N-Labeled Phe (50 mg/liter) was added after 15 min. The cells were grown at 37 °C up to an absorbance of 0.8–1.0 at 600 nm and induced with 1 ml of 1 M isopropyl 1-thio-$\beta$-D-galactopyranoside. The incubation temperature was reduced to 28 °C and a speed of 180 rpm following which a second portion of $^{15}$N-labeled Phe (50 mg/liter) was added to it after 30 min. The culture was allowed to grow further for 40 h.

*Purification of $^{15}$N-Phe-labeled Proteins*—The cells were harvested by centrifugation at 5000 rpm at 4 °C for 20 min, and the pellet was resuspended in 4 ml/g cell of 50 mM PBS, pH 8.0, containing 20 mM imidazole and 500 mM NaCl, 1 mg/ml lysozyme, 1 mM phenylmethylsulfonyl fluoride, 10 mM $\beta$-mercaptoethanol, and 1 tablet of protein inhibitor mixture (Roche Applied Science). The cells were stirred on ice for 30 min followed by sonication using a Branson sonicator (five 45-s bursts at 50% power, with 2 min cooling in an ice bath between each burst) to promote lysis of the cells. The suspension was then centrifuged in a Sorvall Ultracentrifuge (45 Ti rotor) at 35,000 rpm for 2 h at 4 °C to separate cellular debris from protein. The protein-containing supernatant was loaded on a nickel-nitrilotriacetic acid column (5 ml of HisTrap HP from GE Healthcare) pre-equilibrated with 20 mM potassium phosphate buffer, pH 7.4, containing 5% (v/v) glycerol, 20 mM imidazole, and 500 mM NaCl. The column was washed with ~5 column volumes of the above mentioned equilibration buffer. The protein was washed with a salt gradient of 20–100 mM imidazole in 50 mM potassium phosphate buffer at pH 7.4 containing 5% (v/v) glycerol and 500 mM NaCl. The protein was then eluted by increasing the concentration of imidazole to 200 mM. The collected protein was dialyzed overnight in a 12-ml cassette against 1 liter of 100 mM phosphate buffer, pH 6.5. The protein was then concentrated using 30,000 molecular weight cutoff Amicon centrifugal filter tubes (Millipore) and stored in at −80 °C. The protein, as judged by SDS-PAGE, was judged to be >90% pure. The final concentration of the ferrous-CO protein was determined using UV-visible spectroscopy, with an extinction coefficient of $\epsilon = 100\ mM^{-1}\ cm^{-1}$ at a wavelength of 450 nm.

*Ligand $K_d$ Determination by Optical Difference Spectroscopy*—To determine the $K_d$ value, UV-visible difference spectra were acquired for various ligands on a Varian Cary 1E UV-visible scanning spectrophotometer. Both the sample and reference chambers contained 500 $\mu$l of 3 $\mu$M CYP119 in 100 mM potassium phosphate, pH 6.5. Prior to initiating the titration, a baseline was recorded between 350 and 500 nm. A 1 M stock of the small molecule ligand to be titrated was prepared in ethanol or 100 mM phosphate buffer, and subsequent stock solutions were prepared by serial dilution in potassium phosphate buffer. Aliquots of the concentrated stock solutions of the ligand were added to the sample cuvette, whereas an equal volume of vehicle solvent was added to the reference cuvette to determine the difference spectrum at varying concentrations (0–100 mM).

The absolute change in absorbance was plotted as a function of ligand concentration.

*$^{1}H,^{15}N$ HSQC NMR Measurements*—$^{1}H,^{15}N$ HSQC spectra were acquired on a Bruker 800 MHz spectrometer equipped with a $^{1}H/^{13}C/^{15}N$ triple resonance cryoprobe with actively shielded pulse-field gradients at 310 K. Spectra were acquired with 72 scans using spectral widths of 12,820 Hz ($^{1}H$) and 3243 Hz ($^{15}N$). Each NMR sample consisted of 200–250 $\mu$l of 0.2–0.25 mM concentrated solution of $^{15}N$-labeled Phe CYP119 protein in a 100 mM potassium phosphate, pH 6.5, buffer with 10% (v/v) $D_2O$ added as a lock solvent placed in a Shigemi tube. For the $^{1}H,^{15}N$ HSQC spectra of ligand-bound protein experiments, aliquots of a concentrated stock solution were added to reach the desired final concentrations for each experiment, and the data were recorded using the above conditions. The final ratio of ligand to enzyme was 2:1. Data processing and analysis were performed with the TopSpin 3.1 software.

*Expression and Purification of CYP119 for Structural Studies*—Initial failures at CYP119 ligand co-crystallization led us to express and purify the enzyme in a *pCWori* vector without a $His_6$ tag. Expression and cell lysis were performed as described previously (38) with some changes in the purification. Briefly, a 40% (w/v) ammonium sulfate cut was applied to the supernatant followed by centrifugation at 6000 rpm for 10 min. A 60% (w/v) ammonium sulfate cut was applied to the soluble fraction, and the mixture was spun down at 6000 rpm for 10 min. The pellet was resuspended in 50 mM BisTris, pH 7.2, and dialyzed into the same buffer overnight at 4 °C. The protein was then loaded onto a DEAE-Sepharose column and eluted in 50 mM BisTris, pH 6.0, and a gradient of 0–250 mM NaCl. Fractions with a 415:280 nm absorbance ratio greater than 1.2 were pooled, and ammonium sulfate was added to a final concentration of 1 M. Protein was then loaded over a *tert*-butyl HIC column, washed with buffer A (50 mM BisTris, pH 6.0, 500 mM ammonium sulfate), followed by increasing concentrations of buffer B (50 mM BisTris, pH 6.0), and eluted in 60% buffer B. Fractions were dialyzed into 50 mM BisTris, pH 6.0. Protein that had a 415:280 nm absorbance ratio greater than 1.5 was pooled, flash-frozen in liquid nitrogen, and stored at −80 °C.

For crystallography, CYP119 was thawed and diluted 20 times into 10 mM Tris with 1, 2.5, or 5 mM ligand (4-BPI, 4-CPI, and 4-FPI, respectively) and incubated at room temperature for 30 min prior to concentrating to 250 $\mu$M. An $\epsilon_{422} \sim 100.5\ mM^{-1}\ cm^{-1}$ for complexes was determined by calculating the concentration of the low spin protein using $\epsilon_{415} = 104\ mM^{-1}\ cm^{-1}$ (39) and titrating in ligand while taking volume changes into account. Concentrations were thereafter calculated using the ligand-bound extinction coefficient.

*Crystallography of 4-BPI and 4-CPI-bound CYP119*—CYP119 crystals were grown in sitting drop vapor diffusion Cryschem™ (Hampton) crystal trays with wells containing 0.7–1 M ammonium sulfate, 340 mM NaCl, 80 mM sodium acetate, pH 4.5, 20 mM sodium acetate, pH 5.6, 22% (v/v) glycerol following a 3-day incubation at room temperature. Each well contained 500 $\mu$l of well solution, 1 $\mu$l of CYP119, and 1 $\mu$l of mother liquor. Crystals were harvested directly from the crystallization drop and frozen in liquid nitrogen prior to data collection. For 4-CPI-bound CYP119, crystals were grown analogously to CYP119 4-BPI crystals except that they required a higher degree of precipitant and a longer incubation time than the latter. The well solution contained 1.3–1.6 M ammonium sulfate, 340 mM NaCl, 80 mM sodium acetate, pH 4.5, 20 mM sodium acetate, pH 5.6, 20% (v/v) glycerol following a 2-week incubation at room temperature.

Data for the CYP119 4-BPI-bound crystal structure were initially collected in-house on an R-axis IV using 1° oscillations and an exposure time of 25 min per frame. Data were scaled and integrated in XDS as P6322. Initial phases and an early round of refinement were determined using Phaser with the previously published 4-PI structure with all the ligands removed. Model building in Coot was used to place the heme and 4-BPI ligand with further refinement performed in phenix.refine implemented in the Phenix package. Following structure solution, higher resolution data were collected at the ALS synchrotron beamline 8.3.2. High and low resolution data were collected in two successive 180° wedges starting from $\phi = 332°$ using 0.7° oscillations. The low resolution data were collected first at a crystal to detector distance of 250 mm for 0.4 s. High resolution spots were captured by a second data collection at 350 mm for 1.7 s. Reflections were integrated and scaled separately using XDS (40). Data were merged and scaled together using 25–2.7 Å for the low resolution data and 3–2.2 Å for the high resolution data. Intensities were converted to structure factors using truncate from the CCP4 package (41) and refined against the model built using our in-house data. Successive rounds of model building and refinement were performed in Coot (42) and phenix.refine (43). The 4-BPI ligand was manually fit into the electron density, subsequently refined using ligand parameters determined from idealized bond and angle distances, and optimized using ELbow as implemented in the PHENIX package (43). All atoms were refined with isotropic B-factors and individual coordinates. Four waters were near special positions and so were fixed with occupancies of 0.5.

Our initial CYP119 4-BPI-bound crystal structure diffracted to ~2.2 Å with excellent $2DF_o - mF_c$ density for the bromine substituent. However, a negative peak in our $F_o - F_c$ electron density map indicated either increased thermal motion or partial occupancy for the bromine atom. It has been shown that bromine atoms, and aryl-bromine derivatives in particular, are among the most sensitive atoms to radiation-induced x-ray damage (44). Given that neighboring ligand atoms exhibited similar B-factors and that the bromine atom is constrained to lie in the plane of the aromatic phenyl moiety, we believe that refining the occupancy of the bromine atom was justified and that the resulting reduced occupancy stemmed from x-ray damage. Therefore, we optimized data collection to avoid such damage with a total estimated x-ray dose of 0.5 Mg$\gamma$ (where Mg$\gamma$ is radiation flux) for the entire data set. Even under these conditions, the bromine atom occupancy refined to ~0.7 with strong negative $F_o - F_c$ density persisting when the occupancy was set to 1.0. Fluorescence scans of the crystal before and after data collection revealed a sharp drop in intensity at the bromine edge over the course of the data collection. These results suggest that a high resolution crystal structure with a fully occupied bromine atom would require a multiple crystal collection strategy. However, given that our 0.5 Mg$\gamma$ data set did not show

any structural differences from our highest resolution structure, we believe it is unlikely that there will be any significant structural changes stemming from the loss of the bromine atom during data collection. Therefore, we chose to use our highest resolution crystal structure for the structural interpretations described under "Discussion."

The CYP119 4-CPI-bound structure was solved analogously to the 4-BPI-bound structure with the following differences. Intensity data were collected at Stanford Synchrotron Radiation Lightsource (Menlo Park, CA) on beamline 7-1 using a Q315R detector and a starting $\phi = 20°$. A total of 200 frames were collected each having an oscillation width of 0.5°. Although we solved the 4-CPI crystal structure in the same unit cell as the 4-BPI-bound CYP119, we used the starting phases from CYP119–4-PI-bound coordinates (PDB code 1F4T) (ligands removed) for molecular replacement to eliminate any potential model bias coming from the 4-BPI-bound structure.

*Room Temperature Crystallography of 4-BPI-bound CYP119*—CYP119–4-BPI crystals for room temperature data collection were prepared exactly as described for collection at 100 K except that the crystals were not flash-frozen. Instead, they were directly mounted onto a MiTeGen MicroGripper™ and transferred to a MiTeGen MicroRT™ capillary for data collection. Fifteen data sets of 20 frames were collected using 0.5° oscillations per frame. A single test shot was used to optimize the attenuation so that each crystal would experience less than 0.2 Mgγ of radiation during the data collection using Raddose16 as implemented in the SSRL Blu-ice interface. Data sets were truncated before sharp increases in $R_{merge}$ suggested radiation damage (typically about 10 frames). The remaining data from multiple crystals were merged and scaled together using XDS (40). Structure solution was carried out as described above.

*Crystallography of 4-FPI-bound CYP119*—We initially tried to grow diffractable crystals using conditions similar to those described for the 4-CPI- and 4-BPI-bound crystal structures. However, we were only able to obtain microcrystals in addition to two crystals large enough to attempt mounting for x-ray diffraction. These crystals had similar morphology to those of bromo and chloro-substituted ligand-bound CYP119; however, they were much more fragile and shattered upon manipulation. Fragments diffracted to only 16 Å. Therefore, we used microcrystals to make seed stocks containing crystallization mother liquor with 1.4 M ammonium sulfate, 80 mM sodium acetate, pH 4.5, 20 mM sodium acetate, pH 5.6, 20% (v/v) glycerol, and 200 mM NaCl. The seed stock was vortexed using a Hampton Seed Bead™ and added to 96-well commercial screens as an additive. The best crystals were obtained by mixing 0.3 μl of seed stock mother liquor (no crystal seeds) and 1 μl of protein (4 mM 4-FPI) with 1 μl of well solution (2% (w/v) PEG 8K, 400 mM $MgCl_2$, and 100 mM $LiCl_2$) in sitting drop vapor diffusion Cryschem™ (Hampton) crystal trays. Crystal seeds were not needed for crystallization; however, the stock ammonium sulfate mother liquor was absolutely required as an additive. Diffraction data were collected at SSRL beamline 7-1 using λ = 1.27, an oscillation width of 0.3° per frame, and a total of 258 frames. Data were initially integrated and scaled in XDS, followed by automated point group checking in pointless and final scaling in Aimless giving 2 molecules in the asymmetric unit and a $P2_12_12_1$ space group. An initial molecular replacement solution was established using Phaser and the 4-PI crystal structure with all ligands removed. Refinement was carried out in phenix.refine using isotropic B-factors, individual coordinates, and NCS torsion restraints for the two molecules in the asymmetric unit. Phenix.refine allows for local differences in NCS torsion between chains by using a target function that is smoothly cut off as the difference between the two chains increase. This allowed us to visualize significant conformational differences in the FG loop between the two chains. To remove potential model bias, an iterative built omit map in which residues 161–165 were omitted using Phenix autobuild in the Phenix GUI (43) and model building in Coot greatly improved our $2DF_o - mF_c$ map in this region. The 4-FPI ligand was modeled using Coot, and ligand restraints were determined as stated above for the 4-CPI ligand. Final statistics can be found in Table 1.

## RESULTS

*UV-visible Monitored Titration of CYP119 with Various Ligands*—UV-visible spectroscopy was used extensively to characterize the binding of ligands within the cytochrome P450 active site. Direct coordination of a ligand heteroatom to the heme iron atom produces a low spin state that is identified by an absorbance increase at 420 nm and a decrease at 390 nm, whereas simple displacement of the normal water ligand from the iron gives rise to a high spin state characterized by the opposite spectral signature. The binding affinity of 17 phenylalanine CYP119 mutants prepared for the NMR resonance assignment was measured with 4-PI, an iron-coordinating ligand, to assess their ligand binding ability. Overall, the mutants had binding affinities similar to the wild-type with the exception of the F228L and F36L mutants, which bound 4-PI ~18 and 9 times more weakly, respectively (Table 2).

The dissociation constants of several azoles and substrates were then determined. In general, the binding affinity of the azoles increases in proportion to the size and lipophilicity of the side chain, as illustrated by the *n*-alkyl-substituted imidazoles (Table 3). However, steric considerations are also relevant, as 1-*tert*-butylimidazole, despite a log *p* value only slightly lower than that of 1-*n*-butylimidazole (log *p* 1.18 *versus* 1.43, respectively), is bound much more weakly ($K_d$ = 50.5 *versus* 2.5 μM, respectively). Azoles with side chains larger than that of 4-PI, including 4-FPI, 4-CPI, 4-BPI, 4-(2-bromophenyl)imidazole (2-BPI), econazole, and ketoconazole, exhibited $K_d$ values between 0.74 and 3.4 μM (Table 3). Moving the phenyl group of 4-PI to the nitrogen, as in 1-phenylimidazole (1-PI), resulted in a 2-fold decrease in binding affinity, in agreement with data reported for CYP2B4 (45). Lauric acid and stearic acid, two substrates, had similar binding constants with CYP119, whereas styrene is only a weak substrate of CYP119 (46). Ligands were chosen for NMR analysis that had $K_d$ values within 50-fold that of 4-PI.

*Two-dimensional $^1H,^{15}N$ HSQC NMR of Ligand-free $^{15}N$-Phe-labeled Fe(III) CYP119*—Analysis by two-dimensional $^1H,^{15}N$ HSQC NMR of ligand-free $^{15}N$-Phe-labeled CYP119 revealed 13 distinguishable resonances designated A to M (Fig.

**TABLE 1**
**Data collection and refinement statistics**
r.m.s.d. is root mean square deviation.

| Data set | CYP119-FPI PDB code 4WPD | CYP119-CPI PDB code 4TUV | CYP119-BPI CRYO PDB code 4TT5 | CYP119-BPI RT PDB code 4WQJ |
|---|---|---|---|---|
| Radiation source | SSRL 7-1 | SSRL 7-1 | ALS 8.3.1 | SSRL 7-1 |
| Space group | P212121 | P6322 | P6322 | P6322 |
| Unit cell dimensions (*a*, *b*, *c*) (Å) | 78.80, 95.46, 106.72 | 165.80, 165.80, 75.86 | 165.34, 165.34, 76.81 | 168.680, 168.68, 76.350 |
| Resolution range (Å) | 38.1–2.00 | 36.7–2.50 | 20 (2.18) | 20 (2.70) |
| Wavelength (Å) | 1.127 | 1.127 | 1.116 | 1.127 |
| Total observations | 200,569 | 269,226 | 1,141,390 | 82,290 |
| Unique reflections (highest shell) | 54,418 (3859) | 21,711 (1559) | (4761) | 17,686 (1258) |
| Completeness (%) (highest shell) | 99.1 (96.6) | 99.9 (99.5) | 99.8 (100) | 97.7 (95.5) |
| CC(1/2) (highest shell) | 99.7 (87.3) | 99.9 (72.0) | 99.9 (91.6) | 99.7 (70.9) |
| $R_{meas}$ (highest shell) | 0.087 (0.422) | 0.104 (1.19) | 0.099 (0.987) | 0.099 (0.758) |
| $\langle I/\sigma \rangle$ (highest shell) | 15.5 (4.0) | 24.5 (2.0) | 31.1 (4.2) | 11.8 (2.9) |
| Redundancy (highest shell) | 3.7 (3.7) | 12.4 (11.3) | 34.9 (24.4) | 4.7 (3.7) |
| B-factor, Wilson plot (Å$^2$) | 24.0 | 51.6 | 41.9 | 64.9 |
| Reflections used in refinement | 54,363 | 21,708 | 32,665 | 19,125 |
| Resolution range (Å) used in refinement | 36.4–2.00 | 36.7–2.50 | 19.86–2.18 | 19.95–2.60 |
| No. of protein atoms fit | 6087 | 3028 | 3029 | 3029 |
| No. of heteroatoms fit | 110 | 54 | 61 | 61 |
| No. of waters fit | 777 | 68 | 199 | 200 |
| $R_{work}$ % | 16.1 | 19.0 | 18.2 | 16.2 |
| $R_{free}$ % | 19.6 | 23.9 | 22.1 | 21.5 |
| r.m.s.d. bond length (Å) | 0.008 | 0.010 | 0.009 | 0.010 |
| r.m.s.d. bond angle (°) | 1.06 | 1.21 | 1.08 | 1.23 |
| Average B, protein atoms | 18.9 | 52.1 | 45.8 | 73.9 |
| Average B, heteroatoms | 10.0 | 37.2 | 33.9 | 57.4 |
| Average B, halide ligand | 13.2 | 39.3 | 35.7 | 64.0 |

**TABLE 2**
**4-PI binding affinity constants for CYP119 mutants**

| CYP119 | $K_d$ | CYP119 | $K_d$ | CYP119 | $K_d$ |
|---|---|---|---|---|---|
| | μM | | μM | | μM |
| WT | 1.1 ± 0.1 | F5L | 2.9 ± 0.2 | F24L | 2.8 ± 0.3 |
| F36L | 9.6 ± 0.6 | F39L | 1.2 ± 0.1 | F60L | 5.0 ± 0.7 |
| F87L | 5 ± 3 | F98L | 0.9 ± 0.1 | F144L | 2.5 ± 0.2 |
| F153L | 1.2 ± 0.1 | F162Y | 1.0 ± 0.1 | F225L | 1.7 ± 0.6 |
| F228L | 20 ± 4 | F292L | 0.8 ± 0.1 | F298L | 1.7 ± 0.1 |
| F310Y | 1.0 ± 0.1 | F334L | 1.0 ± 0.1 | F338Y | 1.9 ± 0.5 |

**TABLE 3**
**Lipophilicity values and binding affinity constants for binding of various ligands to CYP119**

| Ligand | log *p* (calculated) | $K_s$ |
|---|---|---|
| Imidazole | −0.08 | 145 |
| 4-Phenylimidazole | 1.46 | 1.1 ± 0.1 |
| 1-Phenylimidazole | 1.53 | 2.5 ± 0.3 |
| 4-(4-Fluorophenyl) imidazole | 1.97 | 0.7 ± 0.1 |
| 4-(4-Chlorophenyl) imidazole | 2.71 | 1.4 ± 0.1 |
| 4-(4-Bromophenyl) imidazole | 2.89 | 2.0 ± 0.9 |
| 4-Methyl imidazole | 0.31 | 133 ± 21 |
| 4-Bromoimidazole | 0.49 | 147 ± 15 |
| 1-Ethyl imidazole | 0.42 | 39.0 ± 2.4 |
| 1-*n*-Butyl imidazole | 1.43 | 2.5 ± 0.5 |
| 1-*t*-Butylimidazole | 1.18 | 50.5 |
| 4-Hydroxymethyl imidazole | −0.47 | 203 ± 41 |
| Econazole | 5.32 | >1 |
| Ketoconazole | 3.55 | 3.4 |
| Lauric acid | 5.03 | 1 |
| Stearic acid | 8.22 | 1.8 |

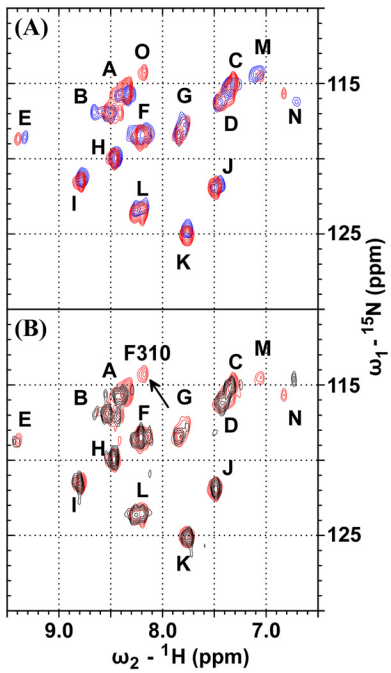


FIGURE 2. **$^1$H,$^{15}$N HSQC overlap spectra of ferric ligand-free (*blue*) and Fe(II)-CO (*red*) of $^{15}$N-Phe-labeled CYP119 (*A*) and Fe(II)-CO (*red*) and Fe(II)-F310Y-CO (*black*) $^{15}$N-Phe-labeled CYP119 (*B*).**

2*A*, *blue*). Their overall dispersion is indicative of a properly folded protein. Dynamic light scattering measurements indicate that the ligand-free protein is monomeric. As there are 17 Phe residues in CYP119, the signals for four Phe residues were absent or unresolved in the spectrum. Signals from these Phe residues may be unobservable due to resonance overlap, H-D exchange, line broadening caused by variable dynamics of these particular regions, or ferric iron paramagnetic effects. Interestingly, resonance E is shifted considerably further downfield in the proton dimension compared with the signals of the other Phe residues, suggesting a significantly deshielded chemical environment, whereas the environment around M is comparatively shielded. Overall, the large number and wide distribution of the resonances detected in this aromatic region of the spectrum indicated the feasibility of monitoring global conformational effects of ligand binding in CYP119 by NMR.

*Two-dimensional $^1$H,$^{15}$N HSQC NMR of Ligand-free, $^{15}$N-Phe-labeled Fe(II)-CO CYP119*—To determine whether a paramagnetic effect of the heme accounts for the missing NMR

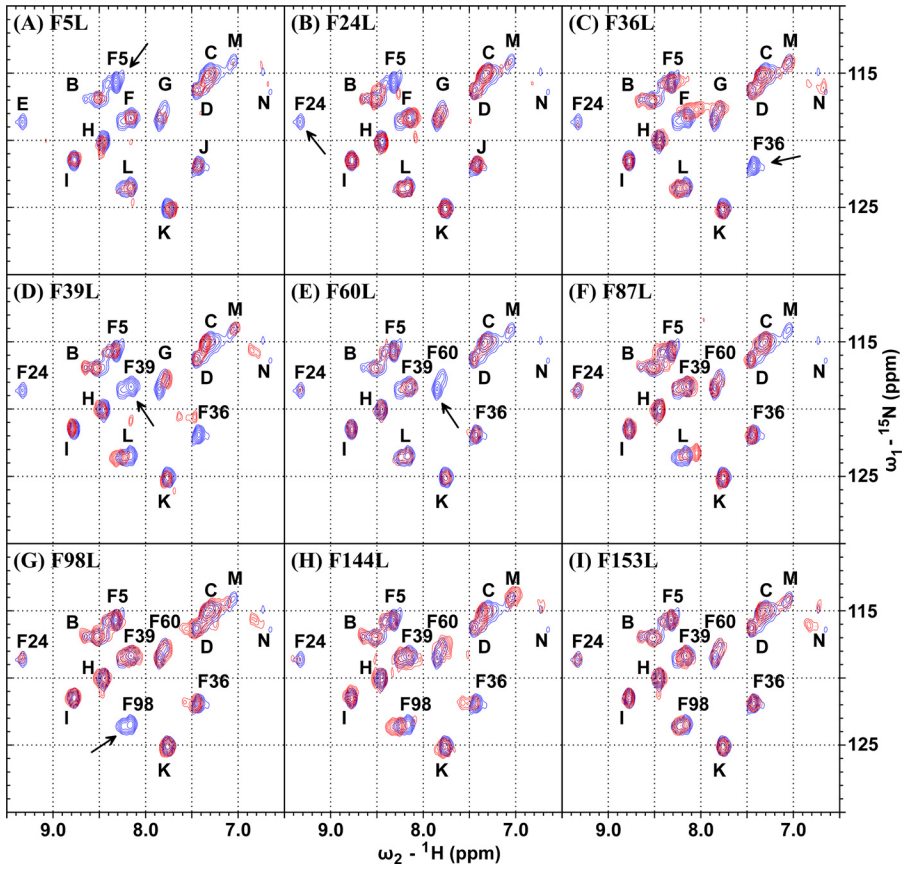


FIGURE 3. **Superimposition of the NMR spectrum of $^{15}$N-Phe-labeled wild-type CYP119 (*blue*) with the indicated $^{15}$N-Phe-labeled mutant (*red*) as follows: *A*, F5L; *B*, F24L; *C*, F36L; *D*, F39L; *E*, F60L; *F*, F87L; *G*, F98L; *H*, F144L; *I*, F153L.**

signals, the NMR of reduced CYP119 bound to CO was investigated. The overall NMR spectrum was similar to that of ferric CYP119 except for the appearance of two new peaks at $^{1}$H = 6.83 ppm, $^{15}$N = 115.7 ppm (N), and $^{1}$H = 8.17 ppm, $^{15}$N = 114.3 ppm (O) (Fig. 2*A*, *red*). In addition, signal E underwent a downfield shift in the proton dimension. The calculated Phe(NH)-Fe distances of Phe-87 and Phe-310 from the CYP119 crystal structure (PDB code 1IO9) are 9 and 5 Å, respectively, which places them among the closest residues to the heme iron atom. Signal O could be assigned to Phe-310 because it disappears in the NMR spectrum of the ferrous F310Y-CO-CYP119 mutant (Fig. 2*B*, *black*). Although M also disappeared, resonance M was weak or absent for many of the other mutants as well. However, even if paramagnetic effects are responsible for the suppression of signals N and O in the ferric protein, the signals of two additional Phe residues remain unobserved and are therefore presumably absent due to factors other than paramagnetic effects.

*NMR Peak Assignments of Phe Residues by Two-dimensional $^{1}$H,$^{15}$N HSQC NMR of Ligand-free Mutants of $^{15}$N-Phe-labeled Fe(III) CYP119*—As reported above, of the 17 Phe residues of CYP119, 15 could be accounted for using $^{1}$H,$^{15}$N HSQC NMR. To assign the signals to specific residues, site-specific mutants were prepared and similarly examined by NMR. Comparison of the spectrum of the ferric, ligand-free F5L-CYP119 mutant with that of the wild type revealed the absence of resonances A and E (Fig. 3*A*). Given the proximity of Phe-5 to Phe-24 in the crystal structure (3.8 Å) (47), disruption of their aromatic interaction provides an explanation for the coupled disappearance of the Phe-24 signal upon mutation of Phe-5. The interaction between these two residues was confirmed by the spectrum of the ligand-free F24L-CYP119 mutant, which also resulted in disappearance of both the A and E resonances. In addition, the broad resonance at B in the F24L mutant spreads upfield in the $^{15}$N dimension, suggesting a merging of peaks A and B (Fig. 3*B*); therefore, A corresponds to Phe-5. To assign peaks A/E as Phe-5/Phe-24 or vice versa, the program SHIFTX (48) was utilized. It suggested that Phe-24 ($^{1}$H = 9.9478, $^{15}$N = 126.4811) is deshielded relative to Phe-5 ($^{1}$H = 7.7633, $^{15}$N = 118.0422), leading to assignment of A and E as Phe-5 and Phe-24, respectively. As the $^{1}$H,$^{15}$N HSQC spectra of many of the mutants did not show the presence of E and N due to their weak intensity, we first focused on the more intense resonances.

Comparison of the spectrum of wild-type CYP119 with the corresponding spectra of the F36L-, F39L-, F60L-, and F98L-CYP119 mutants revealed the absence of resonances J, F, G, and L, respectively, confirming their identity as the signals due to Phe-36, Phe-39, Phe-60, and Phe-98, respectively (Fig. 3, *C–E*, and *G*). The spectrum of the F36L-CYP119 mutant also showed significant displacement of the Phe-39 signal (F) (Fig. 3*C*) and vice versa (Fig. 3*D*), again illustrating the utility of NMR in detecting aromatic interactions.

The spectrum of ligand-free F153L-CYP119 was remarkably similar to that of wild-type CYP119, indicating that the Phe-153

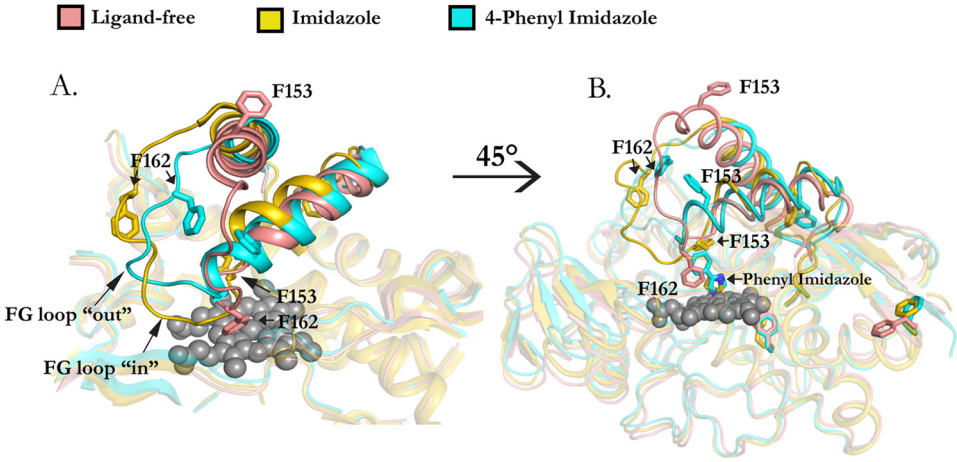


FIGURE 4. ***A*, ligand-free (*pink*, PDB code, 1IO7), imidazole-bound (*yellow*, PDB code, 1F4U), and 4-PI-bound (*cyan*, PDB code, 1F4T) CYP119 aligned by using the heme moiety (*gray spheres*) as a reference.** Selected Phe residues are represented as *sticks*. Residues of interest are labeled. The ligands are not shown. *B*, representation in *A* is rotated counter-clockwise, and the imidazole and 4-PI ligands are shown as *yellow* and *cyan sticks*, respectively.

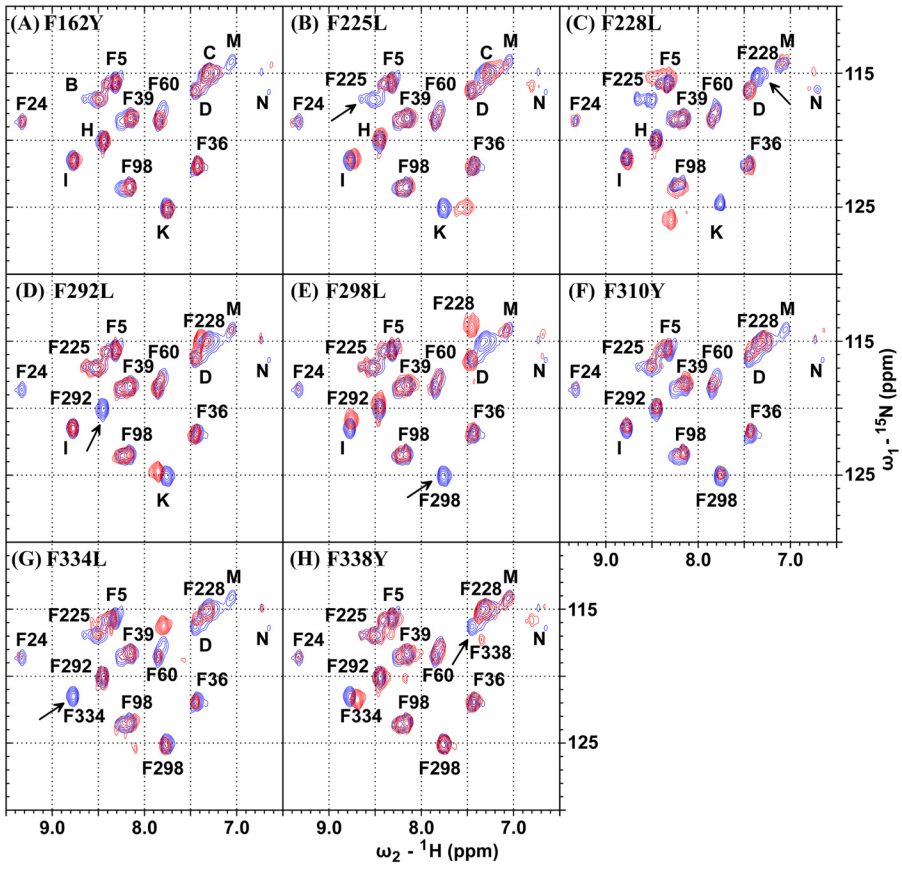


FIGURE 5. **Superimposition of the NMR spectrum of $^{15}$N-Phe-labeled wild-type CYP119 (*blue*) with the indicated $^{15}$N-Phe-labeled mutant (*red*) as follows: *A*, F162Y; *B*, F225L; *C*, F228L; *D*, F292L; *E*, F298L; *F*, F310Y; *G*, F334L; and *H*, F338Y.**

signal is not among the 13 resonances observed in the ferric state (Fig. 3*I*). Interestingly, resonance N was visible in F153L-CYP119, but not in wild-type CYP119, suggesting a proximity of this residue to Phe-153. The resonance peaks were also much sharper compared with the wild type, suggesting a preference for a particular conformation. These observations argue that the Phe-153 residue may not be observed because it is in the highly mobile and solvent-exposed F-G loop (Fig. 4). Like F153L-CYP119, F144L-CYP119 had an NMR spectrum similar to that of the wild type (Fig. 3*H*).

Analysis of ligand-free F225L-, F228L-, F292L-, F298L-, F334L-, and F338Y-CYP119 showed the absence of resonances B, C, H, K, I, and D, respectively (Fig. 5, *B–E*, *G*, and *H*). Many of the Phe residues on the surface are part of aromatic clusters that are thought to contribute to the thermostability of CYP119 (47, 49). Thus, at their closest distance, Phe-225 and Phe-298 are separated by 3.9 Å, Phe-298–Phe-228 by 3.7 Å, and Phe-334–Phe-338 by 3 Å (Fig. 6). As already discussed for Phe-5–Phe-24 and Phe-36–Phe-39, mutation of either Phe-225 or Phe-298 caused significant shifts of the signal of the other residue (Fig. 5,

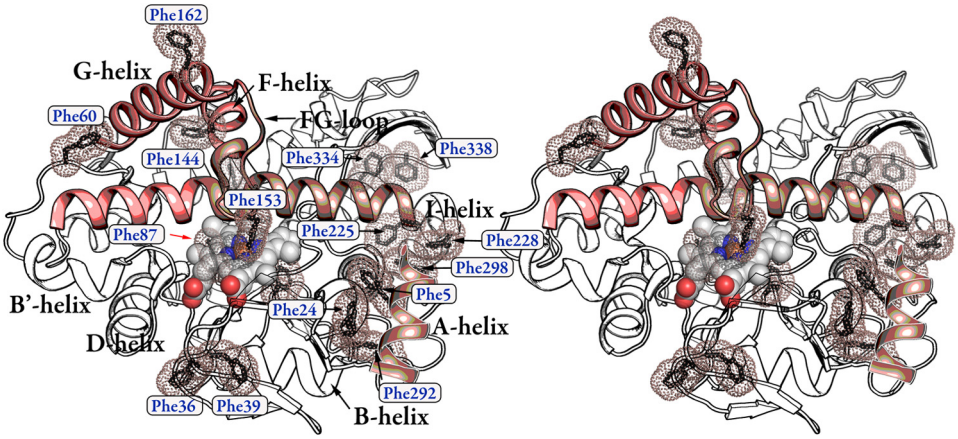


FIGURE 6. **Stereoview of substrate-free CYP119 (PDB code 1IO7).** Phenylalanines are shown as *black sticks* surrounded by *pink dots* representing the van der Waals radii. For emphasis, the F, G, and I helices as well as the F-G loop have been drawn in color, whereas the remaining molecule is colorless. Phe-87 is behind the heme group.

*B* and *E*), whereas an F228L mutation led to disappearance of Phe-225 and displacement of Phe-298 (Fig. 5*C*). The changes in the Phe-334–Phe-338 aromatic pair were less drastic (Fig. 5, *G* and *H*). However, in the $^{1}H,^{15}N$ HSQC spectrum of the F334L mutant, a new residue was observed at $^{1}H = 7.78$, $^{15}N = 116.2$ ppm (Fig. 5*G*). This resonance (*a*) may be that of one of the missing Phe residues that becomes detectable on mutation of Phe-334; (*b*) it may result from complete splitting of the Phe-60 resonance, as the new peak is close to Phe-60 and the Phe-60 resonance is broad in the wild-type spectrum, but in the F334L-CYP119 mutant it appears as a single resonance; (*c*) it may reflect a shift of resonance D to this new position; or (*d*) it may reflect shift of resonance M, which completely disappeared from its original position, to this new position. This ambiguity could possibly be resolved by NMR studies of double mutants, but we have not attempted to do so here as this was not a goal of this study.

Resonance M was also missing in the NMR spectra of the F87L-, F162Y-, and F310Y-CYP119 mutants (Figs. 3*F*, and 4, *A* and *F*). The spectrum of F162Y-CYP119 exhibited a considerable decrease in line broadening of all the resonances, as was observed for the F153L-CYP119 mutant. As these two residues are present in the F-G region and have been found to undergo the greatest degree of displacement in the crystal structures (Fig. 4), their mutation may alter the flexibility of this loop, leading to a decrease in the overall movement of the rest of the protein.

*Two-dimensional $^{1}H,^{15}N$ HSQC NMR of CYP119 Backbone Chemical Shift Perturbations Caused by Fatty Acids and Styrene*—To examine the conformational effects of substrate binding on the CYP119 backbone structure, $^{1}H,^{15}N$ HSQC NMR spectra of CYP119 were recorded with lauric and stearic acids, two relatively high affinity CYP119 substrates ($K_d$ = 1 and 1.8 $\mu$M, respectively), and with styrene, a low affinity substrate. Fig. 7, *A* and *B,* shows titrations of CYP119 with lauric acid and stearic acid, respectively. Interestingly, the resonance M at $^{1}H = 7.08$ and $^{15}N = 114.2$ ppm was more intense in the HSQC spectra with both substrates. The resonance N visible at $^{1}H = 6.8$ ppm, $^{15}N = 115.78$ ppm also had a higher intensity, more so for lauric acid than for stearic acid, which only showed

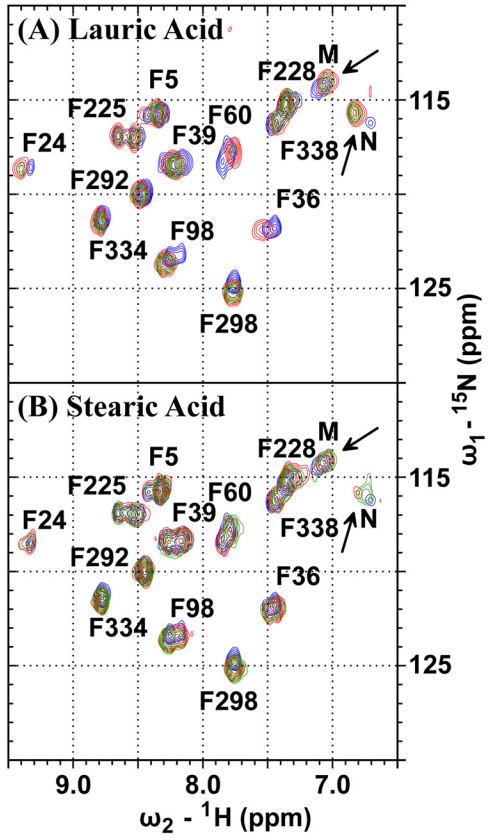


FIGURE 7. **Titration of $^{15}$N-Phe-labeled CYP119 with lauric acid and stearic acid.** $^{1}H,^{15}N$ HSQC spectra monitored at 0.5 (*red*) and 1 (*green*) molar eq of lauric acid (*A*) and 1 (*red*) and 2 (*green*) molar eq of stearic acid superimposed upon the ligand-free protein spectrum (*blue*) (*B*).

a significant peak corresponding to N with 2 eq of stearic acid. Furthermore, signal B corresponding to Phe-225 was split into two resonances shifted farther downfield in the $^{1}H$ dimension. Titration of CYP119 with lauric acid showed movement of Phe-24 (E), Phe-36 (J), Phe-39 (F), Phe-60 (G), and Phe-98 (L) (Fig. 7*A*), implying interaction of the lauric acid chain, either directly or through protein motions, with these residues. The effect was less pronounced for stearic acid (Fig. 7*B*). In contrast, titration with styrene, as expected from earlier work (46),

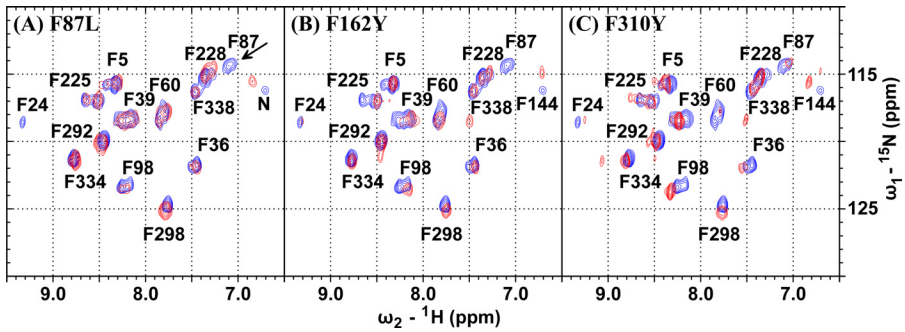


FIGURE 8. **Superimposition of the NMR spectrum of $^{15}$N-Phe-labeled CYP119 (*blue*) with lauric acid-bound $^{15}$N-Phe-labeled (*A*) F87L, (*B*) F162Y, and F310Y CYP119, all in *red* (*C*).**

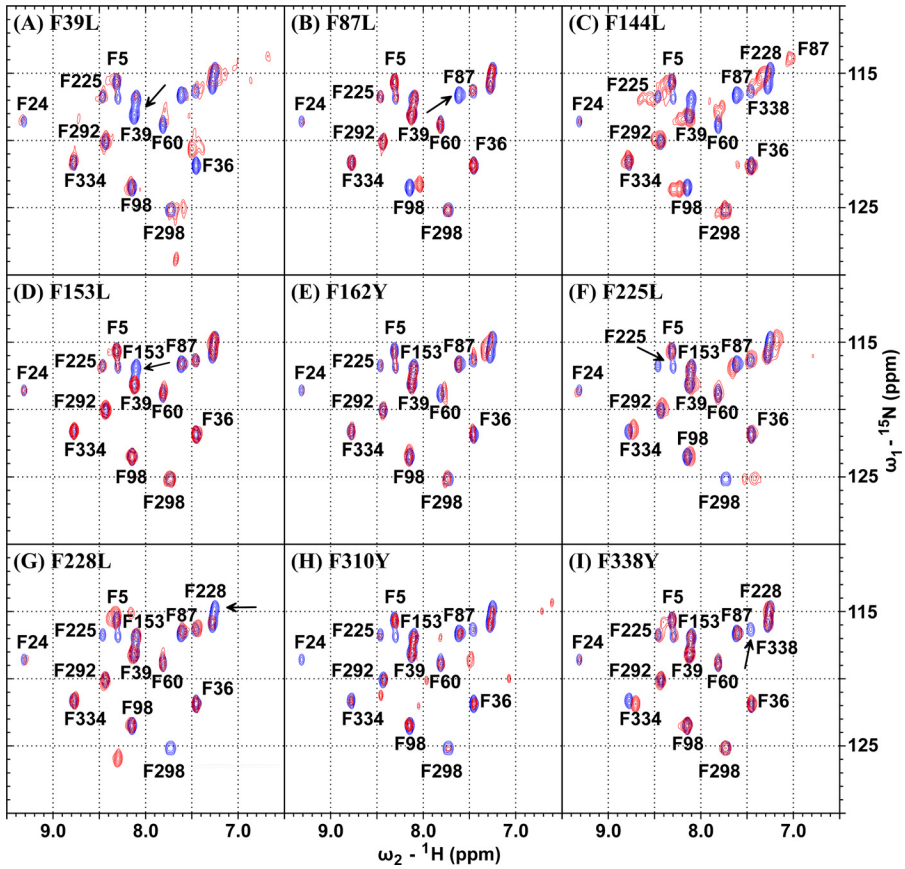


FIGURE 9. **Superimposition of the NMR spectrum of 4-PI-bound $^{15}$N-Phe-labeled CYP119 (*blue*) with those of the following $^{15}$N-Phe-labeled mutants (*red*) as follows: *A*, F39L; *B*, F87L; *C*, F144L; *D*, F153L; *E*, F162Y; *F*, F225L; *G*, F228L; *H*, F310Y; and *I*, F338Y.**

caused no measurable changes in the NMR spectrum (data not shown).

As already mentioned, M was missing and/or low in intensity in the NMR spectra of F87L-, F162Y-, and F310Y-CYP119 (Figs. 3*F*, and 4, *A* and *F*). The increased intensity of the M and N resonances on binding of fatty acids led us to examine the HSQC spectra of the lauric acid-bound, F87L-, F162Y-, and F310Y-CYP119 mutants (Fig. 8, *A*–*C*). Resonance M was assigned to Phe-87 based on the absence of M and the presence of an intense resonance for N at $^{1}$H = 6.83 ppm, $^{15}$N = 115.55 ppm in the NMR spectrum of F87L-CYP119. Additional indirect evidence came from the F98L-CYP119 spectrum (Fig. 3*G*), which showed displacement in the position of M and vice versa (Fig. 3*F*) upon their respective mutations due to their close proximity. Lauric acid-bound F162Y-CYP119 also had a spectrum similar to that of the lauric acid-bound F87L-CYP119 mutant (Fig. 8, *A* and *B*). However, N was shifted to $^{1}$H = 6.71 ppm, $^{15}$N = 114.89 ppm, raising the possibility that M could also be Phe-162. The program SHIFTX (48) predicted values of $^{1}$H = 7.02, $^{15}$N = 117.23 for Phe-87 and $^{1}$H = 8.25, $^{15}$N = 120.92 for Phe-162. These relative values strengthen the assignment of signal M to Phe-87. As the NMR spectrum of the F310Y-CYP119 mutant exhibited both signal M at $^{1}$H = 7.03 ppm, $^{15}$N = 114.15 ppm and signal N at $^{1}$H = 6.82 ppm, $^{15}$N = 115.48 ppm, the resonance N can be assigned to Phe-144 by a process of elimination. This assignment is strengthened by movement of N on mutation of Phe-162 (Fig. 8*B*) and its appearance on mutation of Phe-153 (Fig. 3*I*). Also, SHIFTX

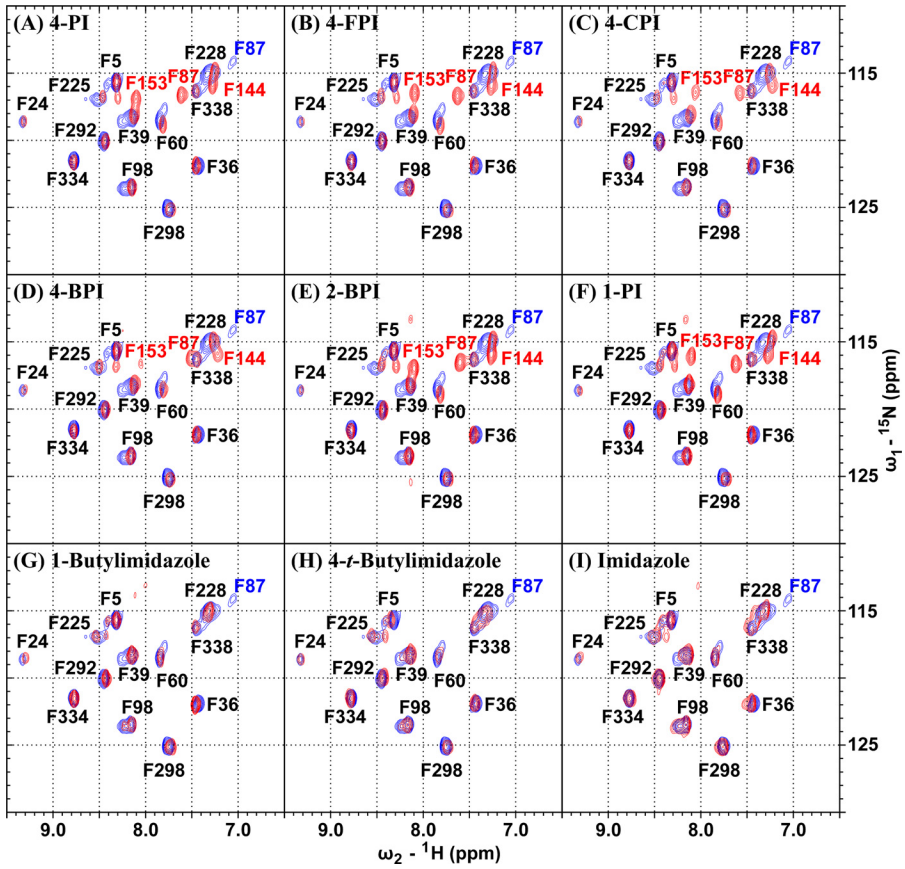


FIGURE 10. **$^{1}$H,$^{15}$N HSQC spectrum of a 1 molar eq of each of the following ligands (*red*) superimposed on the spectrum of the ligand-free protein (*blue*): *A*, 4-PI; *B*, 4-FPI; *C*, 4-CPI; *D*, 4-BPI; *E*, 2-BPI; *F*, 1-PI; *G*, 1-butylimidazole; *H*, 4-*t*-butylimidazole; and *I*, imidazole.**

analysis (48) predicted that the signal of Phe-144 would be at $^{1}$H = 6.6533 and $^{15}$N = 117.7659 ppm, values with a reasonable match to the experimental values.

*Two-dimensional $^{1}$H,$^{15}$N HSQC NMR of CYP119 on Binding of 4-PI*—The $^{1}$H,$^{15}$N HSQC spectrum of CYP119 complexed with the hydrophobic and high affinity CYP119 inhibitor 4-PI (Table 3) was characterized by the appearance of several new resonances (Fig. 10*A*). In agreement with the fact that ligand binding can profoundly impact protein stability and flexibility, the resonance peaks were much sharper in the presence of 4-PI. In particular, resonances Phe-39 (F) and Phe-60 (G) shifted significantly (Fig. 10*A*). Resonance B of Phe-225 was split into two resonances that shifted significantly upfield in the $^{1}$H dimension. The two resonances stemmed from two different conformations of the protein, as neither resonance was present in the HSQC spectrum of the 4-PI-bound F225L CYP119 mutant (Fig. 9*F*). New resonances appeared at $^{1}$H = 8.09 ppm, $^{15}$N = 116.88 ppm, $^{1}$H = 7.59 ppm, and $^{15}$N = 116.57 ppm in the spectra of 4-PI-bound CYP119 (Fig. 9*A*, *red*) compared with wild type (Fig. 9*A*, *blue*). The spectra of the 4-PI-bound F338Y-CYP119 mutant (Fig. 9*I*) confirmed the resonance at $^{1}$H = 7.59 ppm and $^{15}$N = 116.57 ppm as a new resonance that did not result from different conformations of the Phe-338 residue.

As the crystal structures show that Phe-153 and Phe-162 in the F-G loop undergo the largest displacement on ligand binding, the corresponding changes in the HSQC spectra of the respective mutants were determined. Overall, similar chemical shift perturbation patterns were detected on 4-PI binding to F162Y- and F153L-CYP119 as found for the wild-type enzyme, except for the disappearance of the signal at $^{1}$H = 8.09 ppm, $^{15}$N = 116.88 ppm with the F153L mutant, which confirmed its identity as that of Phe-153 (Fig. 9, *D* and *E*). The $^{1}$H,$^{15}$N HSQC spectrum of 4-PI-bound F87L-CYP119 did not exhibit resonance M at $^{1}$H = 7.59 ppm and $^{15}$N = 116.57 ppm that can be assigned to Phe-87 (Fig. 9*B*).

Resonance C of Phe-228 was significantly line-broadened, particularly in the $^{15}$N dimension (Fig. 10*A*), and shifted upfield in the $^{1}$H dimension on binding of 4-PI. The presence of an overlapping resonance was verified by recording the spectrum of 4-PI-bound F228L-CYP119, which retained a sharp signal despite the absence of Phe-228 (Fig. 9*G*). In the presence of 4-PI, both F162Y-CYP119 (Fig. 9*E*) and F310Y-CYP119 (Fig. 9*H*) showed a broad resonance signal at that position similar to that of wild-type CYP119, which rules them out as being responsible for the new resonance adjacent to Phe-228. This resonance may correspond to Phe-144, which disappeared completely from its original position (N) in the presence of 4-PI (Fig. 10*A*). Phe-144, like Phe-87, must therefore undergo a drastic change in environment upon binding of 4-PI. Interestingly, the 4-PI-bound F144L mutant had a spectrum surprisingly similar to that of the ligand-free wild type (Fig. 9*C*). The absence in the mutant of all the NMR characteristics of 4-PI-bound wild-type CYP119 demonstrated the critical role of this residue in mediating the protein changes that are detected by NMR.

*Two-dimensional $^{1}H,^{15}N$ HSQC NMR Chemical Shift Perturbations in $^{15}N$-Phe-labeled CYP119 upon Binding of Imidazole, 1-n-Butylimidazole, and 1-tert-Butylimidazole*—Imidazole is a low affinity CYP119 inhibitor, whereas 1-*n*-butylimidazole and 1-*tert*-butylimidazole have spectroscopic affinities of 2.5 and 50.5 $\mu$M, respectively (Table 3). Titration of these imidazoles into CYP119 caused small chemical shift changes (Fig. 10, *G–I*), notably the disappearance of the Phe-87 (M) resonance and an $^{1}H$ upfield chemical shift of resonance B of Phe-225. Phe-39 (F), Phe-60 (G), and Phe-228 (C) showed significantly less line broadening, as also found for the 4-PI-bound protein. As found for 4-PI binding, the Phe-144 signal (N) disappeared from its resting state position upon binding of imidazole, 1-*n*-butylimidazole, and 1-*tert*-butylimidazole, but unlike binding of 4-PI, it did not merge with the signal of Phe-228.

*Two-dimensional $^{1}H,^{15}N$ HSQC NMR Changes in $^{15}N$-Labeled CYP119 upon Binding of 4-FPI, 4-CPI, 4-BPI, and 2-BPI*—As found for 4-PI (Fig. 10*A*), the binding of 4-FPI, 4-CPI, and 4-BPI caused the Phe-153 signal to appear (Fig. 10, *B–D*). The intensity of the Phe-153 signal increased in going from 4-PI to 4-FPI, followed by a stepwise decrease with increasing size of the *para*-halogen substituent (Fig. 10, *A–D*). Relative to wild-type CYP119, the resonances of Phe-87 (M) and Phe-144 (N) underwent a major repositioning in the HSQC NMR spectra of 4-FPI and 4-CPI comparable with those observed with 4-PI. As the size of the *para*-substituent increased, the signals of Phe-153, Phe-144, and Phe-87 showed an upfield movement, with the Phe-87 resonance almost merging with that of Phe-338 and, in the case of 4-BPI, an extremely weak Phe-153 signal intensity (Fig. 10*D*). When the bromine substituent was moved from the *para*- to the *ortho*-position, the intensity of the Phe-153 signal increased significantly and a shift of the Phe-87 signal occurred, giving rise to an NMR spectrum similar to that obtained with 4-PI (Fig. 10*E*). The binding of 1-PI to CYP119 gave rise to an NMR pattern similar to that of 4-PI with the exception of the Phe-153 signal, which showed an upfield movement in the $^{15}N$ dimension (Fig. 10*F*).

*Two-dimensional $^{1}H,^{15}N$ HSQC NMR of Chemical Shift Perturbations in $^{15}N$-Phe-labeled CYP119 upon Binding of Econazole and Ketoconazole*—Comparable chemical shift perturbation patterns are observed with econazole and ketoconazole. Interestingly, the Phe-60 resonance is shifted upfield in both the $^{1}H$ and $^{15}N$ dimensions at low concentrations of both econazole and ketoconazole, but it then begins to disappear at equimolar ligand/protein concentrations (Fig. 11). Phe-24, which did not substantially change upon titration with imidazole and 4-PI, undergoes a significant shift in both spectral dimensions upon titration with the larger azoles. Phe-36 also exhibits noteworthy chemical shifts with econazole and ketoconazole. However, despite having affinities in the micromolar range, these two large azole compounds did not cause the appearance and/or shift of Phe-153, Phe-144, and Phe-87 observed with 4-PI.

*Crystal Structures of CYP119 Bound to 4-FPI, 4-CPI, and 4-BPI*—The 4-FPI-bound CYP119 structure was very similar to that reported for the 4-PI-bound protein (18), with the exception that in the 4-FPI-bound structure, the residues Glu-160–Glu-163 were rotated by almost 180° in molecule B compared with molecule A of the asymmetric unit. The other difference between the 4-PI- and 4-FPI-bound structures is at Phe-60, which may be due to conformational heterogeneity between the 4-FPI-bound subunits. Phe-60 is a surface residue buried in a crystal contact in the 4-FPI-bound structure, which suggests the rotation is due to crystal packing contacts that are unique in the two molecules within the asymmetric unit.

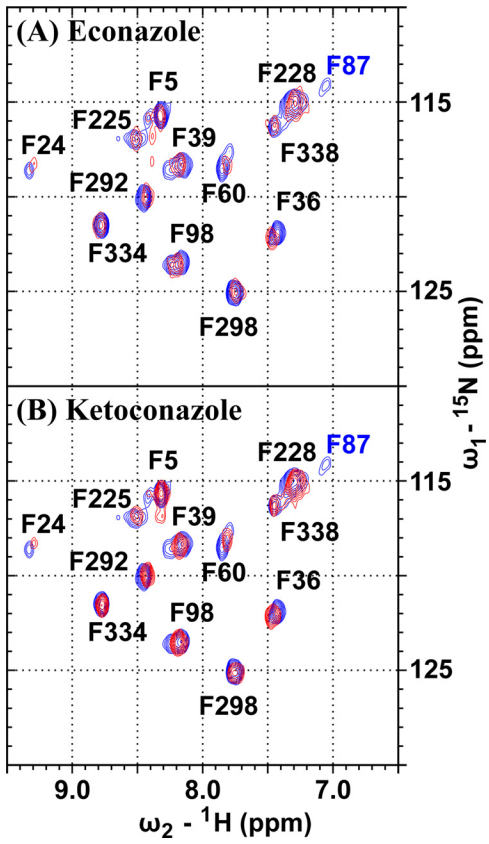


FIGURE 11. **$^{1}H,^{15}N$ HSQC spectrum of a 1-molar eq of each of the following ligands (*red*) superimposed on the ligand-free protein spectrum (*blue*): *A*, econazole; *B*, ketoconazole.**

In the 4-BPI crystal structure, the FG loop is rotated 180° in a kind of "flip-flop" compared with the 4-FPI-bound and previously reported 4-PI-bound structures. Here, the F-helix portion of the loop (residues Ala-152–Lys-157) is rotated away from the 4-BPI ligand, although the G-helix portion of the loop (residues Glu-60–Phe-62) is rotated toward it, resulting in unwinding of the F-helix into a random coil from Val-151 to Gly-165 (Fig. 12). As a result, Leu-155 near the phenyl ring in the 4-PI-bound structure was driven out of the active site in the 4-BPI-bound structure. This movement also caused increased slack in the FG loop, allowing Ile-161 to dive down into the active site and make van der Waals interactions with the $\pi$ orbitals of the 4-BPI phenyl group. Ile-161 is flanked by Phe-162 and is thus sandwiched between two phenyl aromatic rings (Fig. 13). Thus, the loss of the phenyl-Val-155 interaction is compensated for by a gain in van der Waals interactions and a C–H-$\pi$ bonding network with the Ile-161–Phe-162 dipeptide and the 4-BPI ligand. Aside from these alterations, a majority of the protein-ligand interactions are conserved between the 4-PI- and 4-BPI-bound structures, as they involve regions of the protein that are little

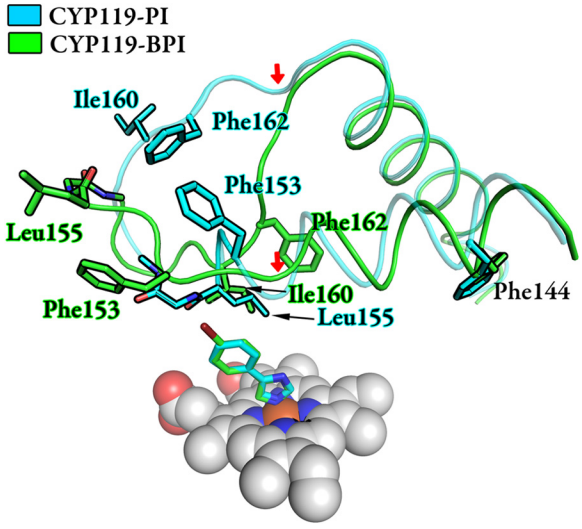


FIGURE 12. **F and G helices of 4-PI-bound CYP119 (*cyan*) overlaid with the 4-BPI-bound CYP119 helices (*green*) using the heme as a reference (*gray spheres*).** Selected residues and a portion of the backbone running through Gly-156 are drawn as *sticks*. For clarity, the 4-PI-bound F and G backbone has been represented as semi-transparent. *Red arrows* denote the point at which 4-(4-bromophenyl)-1*H*-imidazole-bound CYP119 shows the greatest deviation from the phenyl imidazole-bound structure.

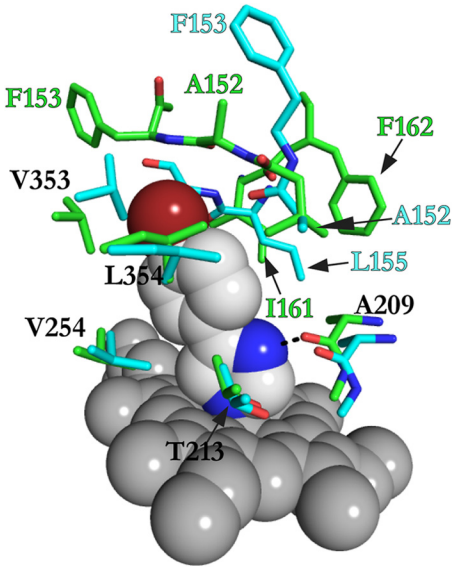


FIGURE 13. **Overlay of the 4-BPI-bound (*green*) CYP119 structure with the 4-PI-bound (*cyan*) CYP119 structure.**

altered by the binding of two ligands despite the large rearrangement in the FG loop.

The 4-CPI-bound CYP119 crystal structure is almost completely analogous to the 4-BPI-bound structure. In Fig. 14, it can be seen that the 4-CPI-CYP119 (*magenta*) backbone as well as Phe residues differ very little from those of 4-BPI-CYP119 (*green*). There is only a small change in that the 4-CPI ligand rotates slightly toward the FG loop, which is probably to lower the steric interaction of the chlorine *versus* bromine substituent. It has been shown that freezing the crystals can compress structures and result in significant differences between room temperature and cryo-cooled structures (50, 51). As the NMR data were recorded at 310 K, we solved a multicrystal room temperature structure to investigate whether higher temperature would engender conformational changes more relevant to the NMR experiments. However, with an overall C-$\alpha$ root mean square deviation of less than 1 Å, the room temperature crystal structure was almost identical to that of the cryogenically obtained structure.

## DISCUSSION

A superposition of published CYP119 crystal structures reveals that Phe-144, Phe-153, and Phe-162 of the FG loop, as well as Phe-60 of the BC loop, undergo displacements of 1.3 to 12 Å, whereas the average Phe backbone displacement is less than 0.85 Å (18, 47). Although the I-helix did not undergo substantial changes in the three reported crystal structures (47), this highly conserved region, which in CYP119 contains Phe-225 and Phe-228, is found in other cytochrome P450 enzymes to play an important role in ligand binding (52, 53). Furthermore, Phe-87 of the CD loop is a conserved residue located near the heme in cytochrome P450 enzymes that moves in transitioning from an open to a closed ligand-bound structure in, for example, the binding of 4-CPI to CYP2B4 (54). In the ensuing discussion, we focus on Phe-87, Phe-144, Phe-153, Phe-162, Phe-225, and Phe-60 of CYP119, as these residues appear to be particularly sensitive probes of ligand binding.

The ligand-free resting state of CYP119 was chosen as the basis state for residue assignment and ligand binding studies. However, to assess the extent of paramagnetic signal broadening for residues close to the ferric heme, dithionite-reduced, CO-bound CYP119 was also examined. The most significant differences between the Fe(III)-$H_2O$ and Fe(II)-CO CYP119 proteins is the presence of new resonances N and O assigned, respectively, to Phe-144 and Phe-310 (Fig. 2*A*). The broadening of some NMR peaks in both the Fe(III)-$H_2O$ and Fe(II)-CO spectra ruled out a paramagnetic effect as the underlying cause for broadening, suggesting that multiple conformations undergo slow exchange in the NMR time scale, as suggested previously for CYP101 (55). Apart from appearance of the N and O signals, the ligand-free CYP119 and Fe(II)-CO-CYP119 had very similar spectral properties, in agreement with their very similar crystal structures (47).

When $^{15}$N-Phe-labeled CYP119 was titrated with imidazole, very little change was evident in the $^{1}$H,$^{15}$N HSQC spectrum (Fig. 10*I*), with the exception of the disappearance of the Phe-87 (M) resonance and separation of the Phe-225 (B) resonance into a doublet that is shifted upfield in the proton dimension. The splitting of the signal of Phe-225, an I-helix residue, at higher imidazole concentrations may reflect a slow-exchange regime between imidazole-bound and imidazole-free CYP119, whereas the upfield shift of the signal is likely to reflect the change in the environment due to close interaction of the I-helix with the ligand. The absence of significant backbone chemical shift perturbations suggests the CYP119 conformation is similar to that of the ligand-free state, with the F-G region fluctuating between open and closed conformations, as evidenced by the absence of the Phe-144, Phe-153, and Phe-162 resonances (Figs. 2*A* and 9*I*). This is consistent with our previously proposed CYP119 imidazole binding model, in which there is a competition between the weakly bound imidazole ligand and water for occupancy of the heme sixth axial position (34). Dou-

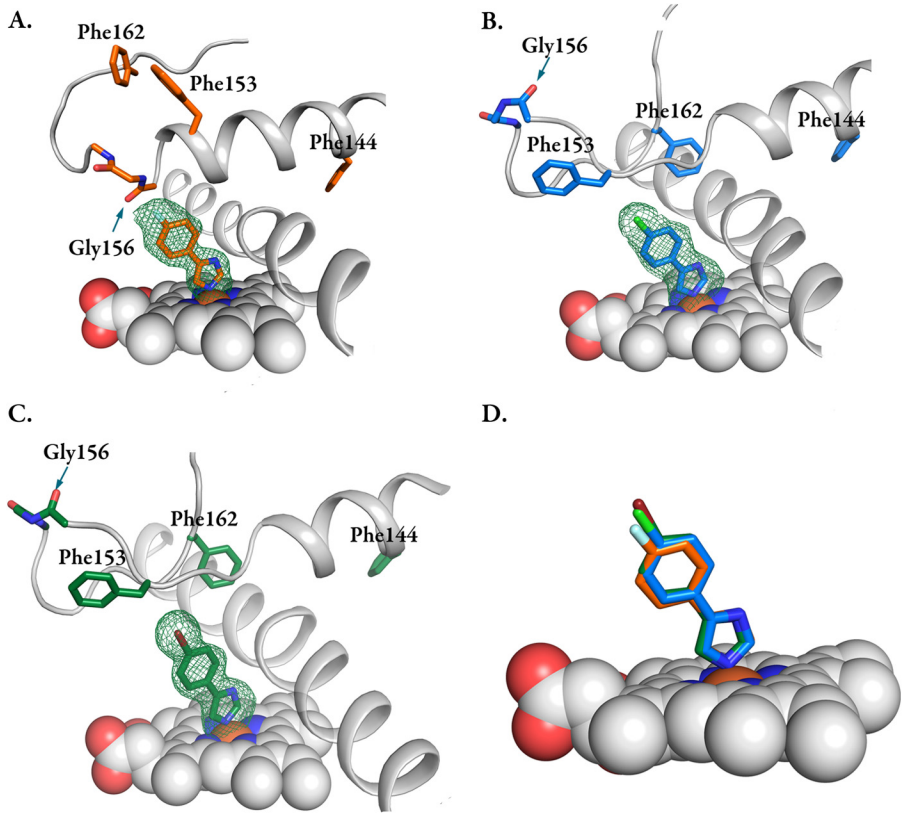


FIGURE 14. **Simulated annealing $F_o - F_c$ omit electron density maps surrounding ligands are shown in *green*.** The $F_o - F_c$ map was contoured to 2 $\sigma$. Ligands for 4-FPI (*A*), 4CPI (*B*), 4-BPI (*C*), and selected Phe residues are drawn as *sticks*. The heme moiety is represented by *spheres*. A portion of the protein backbone, including Gly-156, has been drawn as *sticks*. *D*, three halogenated ligands, 4-FPI (*orange*), 4-CPI (*blue*), and 4-BPI (*green*), are aligned using the heme moiety as a reference.

ble electron-electron resonance studies of $P450_{cam}$ recently showed that its active site in solution in the substrate-free state is in an open conformation (56), in agreement with our NMR findings for substrate-free CYP119. However, in the reported imidazole-bound CYP119 crystal structure (Fig. 4) (Protein Data Bank code 1F4U) (18), the FG loop containing Phe-153 undergoes a large displacement relative to the resting state structure (Protein Data Bank code 1IO9) (47), and Leu-155 approaches the imidazole ligand to within van der Waals distance. There is also a large movement of Phe-162, but this residue does not contact the imidazole ligand and probably is very flexible in solution. The imidazole ligand makes very few direct contacts with the CYP119 backbone or side chains, with the largest interaction probably coming from the heme itself. This is reminiscent of 4-CPI binding to CYP2B4, where there are also scant protein contacts with the imidazole portion of the ligand (54). This interpretation is supported by the lack of a Phe-162 signal in the $^{1}H,^{15}N$ HSQC NMR spectrum of either the ligand-free or imidazole-bound states and by the relatively small deviations in the $\Delta\delta(^{1}H,^{15}N)$ chemical shifts in the spectrum (Fig. 10*I*). However, given the movement observed in the crystal structures, an NMR chemical shift for Phe-153 might have been expected. As imidazole does not have significant protein interactions, there may be no energetic barriers restricting the FG and BC loops from sampling alternative conformational states on the NMR relaxation time scale. This could allow the FG and BC loops considerable flexibility in the binding of small ligands. The precise position of the FG loop in the imidazole-bound CYP119 crystal structure therefore probably reflects the most thermodynamically stable conformation under the crystallization conditions and not the range of conformations accessible in solution (57, 58). NMR methods have sometimes revealed additional states that are not adequately captured in crystal structures (19, 20).

In contrast, binding of the high affinity inhibitor 4-PI to CYP119 causes substantial chemical shifts in the HSQC spectrum (Fig. 10*A*), in accord with the dramatic rearrangement of the protein backbone seen in the crystal structure (18, 47). A high degree of active site structural rearrangement was suggested by appearance of the Phe-153 resonance and displacement of the signals for both Phe-87 (M) and Phe-144 (N). In the crystal structure, a hinge motion pivots the hydrophobic F/G loop into the active site such that part of this loop, including Phe-153, becomes part of the F-helix. This results in a flipping of the orientation of Phe-153 (59). However, although Phe-153, Phe-162, and Phe-144 show significant physical movement in the crystal structure, Phe-87 shows little displacement. However, this residue is known for its proximity to the substrate in $P450_{cam}$ and $P450_{BM3}$ (25, 60, 61), and it may be similarly positioned in the CYP119-substrate complex, for which no structure is yet available. The NMR of CYP119 with lauric and stearic acids, both of which are substrates, exhibited increased intensity of Phe-87, suggesting that this residue has access to alternative conformations in solution (Fig. 7, *A* and *B*). Despite

the large displacement of Phe-153 in the crystal structure with 4-PI, the residue makes no contact with the ligand. Instead, 4-PI is surrounded by hydrophobic van der Waals interactions with the side chains of Ala-152, Leu-155, Ala-209, Val-353, and Leu-354 as well as the backbone atoms of Leu-155, Gly-156, and Gly-210, all of which are within 5 Å of the 4-PI ligand. Therefore, it is not surprising then that the wild-type and F153L mutant exhibit similar affinity for the 4-PI ligand (Table 2). It is worth noting that a van der Waals interaction between Phe-153 and Phe-162, two residues that are 4.2 Å apart and rotated 90° with respect to each other in the 4-PI-bound structure, may help to stabilize the ligand-bound conformation. This interaction may compensate energetically for the loss of the Phe-153-heme interaction present in the substrate-free crystal structure. Moreover, the Phe-225 (B) signal splits into a doublet that is shifted upfield in the proton dimension, as was found on imidazole binding (Fig. 10*I*). The similar results for this particular I-helix residue argue for a similar binding mode to that of imidazole, in agreement with the heme coordination observed by UV-visible spectroscopy. Furthermore, the relatively narrow line widths of the resonance peaks in comparison with those seen with imidazole suggest a slow exchange regime for 4-PI, which would be consistent with its nature as a high affinity ligand.

Interestingly, titration of $^{15}$N-F144L-CYP119 with 4-PI (Fig. 9*C*) did not lead to changes characteristic of 4-PI binding to wild-type enzyme (Fig. 10*A*) even though the ligand-binding constant was 2.5 and 1.1 $\mu$M respectively (Table 2). In the 4-PI-bound crystal structure, the F-helix starts at Asp-140, although in the wild-type protein it starts at Pro-137. Phe-144, located close to the hinge between the movable F-G region and the rest of the protein, seems to play an important role in the ligand-bound conformation by interacting with both Phe-87 (C-D loop, 12.3 Å) and Phe-153 (F-G loop, 12.3 Å). The NMR data suggest significant movement of Phe-87, Phe-144, and Phe-153 in solution, but only Phe-153 showed a significant displacement in the crystal structure. These residues may be spatially closer in solution and may interact with each other, affording the $^{1}$H,$^{15}$N HSQC NMR peaks that are disrupted upon mutation of Phe-144.

Based on the CYP119 structural changes observed with imidazole and 4-PI in the crystal structures (18) and by NMR, a series of azole-based ligands (4-methylimidazole, 1-ethylimidazole, 4-bromoimidazole, 4-(hydroxymethyl)imidazole, 1-*n*-butylimidazole, 1-*tert*-butylimidazole, 1-PI, 4-FPI, 4-CPI, 4-BPI, 2-BPI, econazole, and ketoconazole) were examined to investigate the relationship between ligand size, binding affinity, and the ability to induce the conformational changes detected by NMR. As the size of the ligand was increased from imidazole to 4-methylimidazole and 1-ethylimidazole to 1-*n*-butylimidazole, a proportional increase in binding affinity was observed (Table 3). This can be attributed primarily to the increased lipophilicity of the ligands, although a strict relationship was not observed when affinity was plotted against lipophilicity.

The NMR spectrum for the binding of 1-*n*-butylimidazole ($K_d$ = 2.5 $\mu$M) to CYP119 was similar to that for the binding of imidazole. This suggests that the flexible side chain of 1-*n*-butylimidazole is accommodated within the active site without causing much rearrangement of the F-G loop. To decrease the side chain flexibility, the binding of 1-*tert*-butylimidazole ($K_d$ = 50 $\mu$M) was examined. This compound again gave NMR spectra similar to those obtained with imidazole and 1-*n*-butylimidazole.

Surprisingly, the larger econazole and ketoconazole ligands, which bind to CYP119 with affinities similar to 4-PI (1 and 3 $\mu$M, respectively; Table 3), gave similar chemical shift perturbations ($\Delta\delta(^{1}H,^{15}N)$) in their $^{1}$H,$^{15}$N HSQC (*e.g.* Phe-225, Phe-228, Phe-36, and Phe-60) yet lacked the dramatic NMR shifts of Phe-153, Phe-144, and Phe-87 observed on 4-PI binding. This suggests that econazole and ketoconazole are tightly bound with a CYP119 protein conformation that closely resembles that of the enzyme with water or a small imidazole as the iron ligand (Fig. 11). The fact that the Phe-87 (M) NMR peak disappears on binding of azoles compared with resting-state CYP119 hints that some local differences occur near the proximal side of the enzyme on binding of these ligands.

To define more precisely the influence of subtle structural changes and modest increases in steric bulk, the binding of 1-PI, 4-FPI, 4-CPI, 4-BPI, and 2-BPI was examined. The binding of 1-PI to CYP119 gave an NMR pattern similar to that obtained with 4-PI, as might be expected from their similar size and lipophilicity. However, the Phe-153 signal was upfield in the $^{15}$N dimension for 1-PI relative to 4-PI (Fig. 10, *A* and *F*). This difference may correspond to an increase in active site volume such as that seen in CYP2B4, in which the active site volume in the presence of 1-CPI was greater than with 4-CPI (62), and with the slight change in conformation previously observed on binding of ligands of various sizes to $P450_{cam}$ and CYP2B4 (62, 63).

Titration of $^{15}$N-Phe-WT-CYP119 with 4-(4-halophenyl)-imidazoles gave an NMR signature similar to that obtained with 4-PI (Fig. 10). This was consistent with the finding of similar binding affinities for the 4-(4-halophenyl)imidazoles and 4-PI, suggesting that the active site easily accommodated the *para*-halo substituent. However, the larger bromine substituent led to partial disappearance of the Phe-153 signal and partial shifting of the Phe-87 and Phe-144 signals. Moreover, the intensity of the Phe-153 signal was more intense for the *para*-F compound than for 4-PI and then gradually decreased as the *para*-substituent increased in size from Cl to Br. In contrast, the Phe-87, Phe-144, and Phe-153 NMR resonances with 2-BPI were comparable with those for 4-PI. This suggests that increased bulk at the *para*-position was primarily responsible for a structural rearrangement in CYP119. The crystal structure for 4-BPI-bound CYP119 shows a large structural rearrangement in which the FG helix is flipped compared with its position in the 4-PI-bound structure (Fig. 13). The increase in bulk at the *para*-position thus functions as a conformational switch that is triggered by the potential clash of the bromine substituent with the CYP119 backbone (Leu-155 to Lys-157) that would be present had the enzyme adopted the conformation taken in the 4-PI-bound crystal structure (Fig. 13). It is significant that rather than retracting gradually away from the increasingly large substituent, a major rearrangement of the FG loop occurs to give a new conformation. This finding supports the view that

there are multiple discrete conformations available to the substrate-free enzyme.

In contrast, the 4-FPI-bound CYP119 crystal structure was almost identical to that of the 4-PI-bound enzyme. The smaller size of the fluorine atom is apparently not sufficient to trigger the structural change seen with the larger bromo substituent. However, there was a difference in the NMR on binding of 4-PI *versus* 4-FPI. This question can be addressed by a comparison of the crystallographic B-factors, which report on thermal motion in x-ray crystal structures. Although comparisons between crystal structures can be deceptive, it is appropriate to compare the FG loop B-factors in each structure to its own average B-factor to understand the relative flexibility between the enzymes. When the B-factors are normalized to the average value, the FG loop of 4-FPI-CYP119 has significantly higher B-factors than the 4-PI- or 4-CPI-bound structures (Table 1). In addition, the conformational heterogeneity between the FG loops (Fig. 13) in the two monomers of the asymmetric unit suggests that there is considerably more flexibility in this region in 4-FPI-bound CYP119 compared with the 4-PI-bound enzyme. Furthermore, although we could obtain crystals with 4-FPI under the same conditions as for the 4-BPI-bound enzyme, they diffracted to only 15 Å. Thus, in the case of 4-FPI there may be both conformers (4-PI- and 4-BPI-bound) in solution, but only the former produces a stable crystal structure. This would explain the differences in NMR between the 4-PI- and 4-FPI-bound enzymes.

The 4-CPI-bound enzyme exhibited an almost identical structure to the 4-BPI-bound structure. However, the 4-CPI crystals were much harder to grow and diffracted to lesser resolution (2.7 *versus* 2.1) with much higher B-factors compared with the 4-BPI-bound crystals. It is likely that this high disorder is due to higher flexibility or instability of the 4-CPI-bound than 4-BPI-bound structure. This concurs with NMR data, which shows changes halfway between those of the 4-FPI- and 4-BPI-bound structures, indicating a heterogeneous solution state in which the 4-CPI-bound structure may exist in conformations corresponding to both the 4-PI- and 4-BPI-bound states.

Our results confirm the utility of NMR in distinguishing between the binding of a substrate and an iron-coordinating (type II) inhibitor. When $^{15}$N-Phe-labeled CYP119 was titrated with two different fatty acid substrates, a quite different chemical shift perturbation pattern was observed than on titration with azole compounds (Figs. 7, 10, and 15). The resonances of Phe-24 (E), Phe-36 (J), Phe-39 (F), Phe-60 (G), Phe-98 (L), and Phe-225 (B) of the lauric acid-bound protein were significantly perturbed relative to those of the imidazole- and 4-PI-bound proteins (Fig. 15). Phe-228 (C), which is in the I-helix, was also considerably shifted in the 4-PI-bound spectrum (Fig. 15*B*). The shifts were similar but less drastic with stearic acid (Fig. 7*B*). Furthermore, the intensities of Phe-87 (M) and Phe-144 (N) were increased for both fatty acids, probably due to restricted movement on interaction with the fatty acids. In the NMR spectrum of the wild-type protein, the Phe-60 signal G is asymmetric and broad, which suggests the presence of multiple protein conformations, whereas a narrower signal for this residue in the fatty acid and azole-bound proteins suggests that they are constrained to a single or more limited range of conformations. Moreover, the conformations populated in the presence of fatty acids and inhibitors are different (Fig. 15). Another distinguishing feature is the movement of Phe-87 (M) and Phe-144 (N) on type II binding, whereas their intensity increases without changing position with noncoordinating (type I) ligands. As Phe-225 is located on the I helix that undergoes significant displacement in both the azole-bound crystal structure and HSQC NMR, it is not surprising that its signal shifts downfield in the presence of fatty acids. Qualitatively, many of the resonances are shifted considerably downfield upon substrate binding, giving the overall spectrum a unique fingerprint that distinguishes between type II binding inhibitors and type I substrates (or inhibitors).

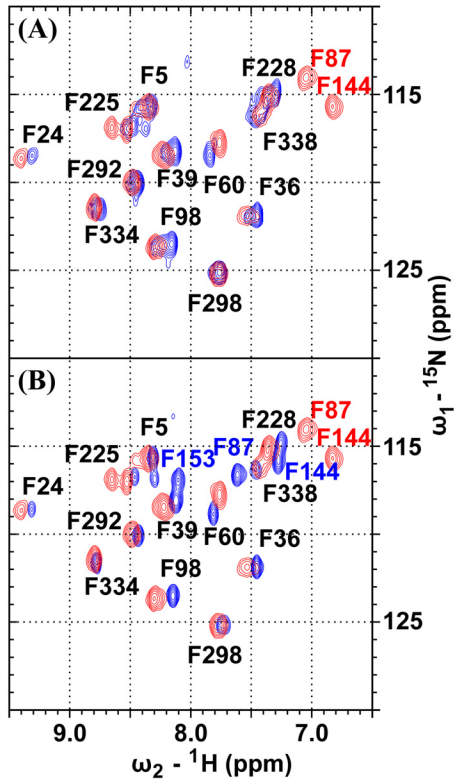


FIGURE 15. **$^{1}$H,$^{15}$N HSQC spectra of $^{15}$N-Phe-labeled CYP119 with lauric acid (*red*) superimposed on those of the imidazole-bound (*A*) and 4-PI-bound (*B*) proteins (*blue*).**

In conclusion, two-dimensional $^{1}$H,$^{15}$N HSQC chemical shift perturbation studies provide new insight into the structural changes associated with CYP119 ligand binding. Movement of only a few specific residues close to the active site regardless of the type of ligand suggests that conformational changes are largely localized to the active site, whereas the rest of the protein undergoes relatively little deformation, a view supported by molecular dynamics simulations (64) and crystal structures. The absence of NMR-detectable displacement of the general protein backbone in the presence of both small and large azole ligands suggests that the protein in solution is largely in an open conformation similar to that of substrate-free CYP119. Binding of certain ligands, notably 4-arylimidazoles, results in a large conformational rearrangement of the FG loop and increases in the size of the *para*-substituent lead to a flipping of the FG loop. Our results provide support for the exis-

tence of defined, discrete conformations of CYP119. Furthermore, the two-dimensional NMR study of CYP119 mutants confirms the previously proposed aromatic stacking interactions in CYP119 (47, 49). In a more global sense, our results demonstrate the utility of NMR in investigations of the conformational states of cytochrome P450 enzymes.

*Acknowledgments—We thank Dr. Christopher Waddling, manager of the X-ray Structure Facility (University of California at San Francisco), and Dr. James Holton and George Meigs of the Advance Light Source beamline (8.3.1), for their help. The Advanced Light Source is supported by Contract DE-ACO2–05CH11231 and the Stanford Synchrotron Radiation Light Source by Contract DE-ACO2–76SF00515, both from the United States Department of Energy. The SSRL Structural Molecular Biology Program is supported by the Department of Energy Office of Biological and Environmental Research and National Institutes of Health Grant P41GM103393.*

## REFERENCES

1. Nebert, D. W., and Dalton, T. P. (2006) The role of cytochrome P450 enzymes in endogenous signalling pathways and environmental carcinogenesis. *Nat. Rev. Cancer* **6,** 947–960
2. Ingelman-Sundberg, M. (2004) Pharmacogenetics of cytochrome P450 and its applications in drug therapy: the past, present and future. *Trends Pharmacol. Sci.* **25,** 193–200
3. Martinez, C. A., and Rupashinghe, S. G. (2013) Cytochrome P450 bioreactors in the pharmaceutical industry: challenges and opportunities. *Curr. Top. Med. Chem.* **13,** 1470–1490
4. Hopkins, A. L., and Groom, C. R. (2002) The druggable genome. *Nat. Rev. Drug Discov.* **1,** 727–730
5. Wackett, L. P. (1998) Directed evolution of new enzymes and pathways for environmental biocatalysis. *Ann. N.Y. Acad. Sci.* **864,** 142–152
6. Ball, A., and Truskewycz, A. (2013) Polyaromatic hydrocarbon exposure: an ecological impact ambiguity. *Environ. Sci. Pollut. Res. Int.* **20,** 4311–4326
7. Strolin Benedetti, M., and Bani, M. (1999) Metabolism-based drug interactions involving oral azole antifungals in humans. *Drug Metab. Rev.* **31,** 665–717
8. Murray, M., and Ryan, A. J. (1983) The binding to oxidised cytochromes P-450 and inhibition of mixed-function oxidases by aryl-substituted benzimidazoles and related compounds. *Chem. Biol. Interact.* **43,** 341–351
9. Loose, D. S., Kan, P. B., Hirst, M. A., Marcus, R. A., and Feldman, D. (1983) Ketoconazole blocks adrenal steroidogenesis by inhibiting cytochrome P450-dependent enzymes. *J. Clin. Invest.* **71,** 1495–1499
10. Howell, A., Cuzick, J., Baum, M., Buzdar, A., Dowsett, M., Forbes, J. F., Hoctin-Boes, G., Houghton, J., Locker, G. Y., and Tobias, J. S. (2005) Results of the ATAC (Arimidex, Tamoxifen, Alone or in Combination) trial after completion of 5 years' adjuvant treatment for breast cancer. *Lancet* **365,** 60–62
11. Jakesz, R., Jonat, W., Gnant, M., Mittlboeck, M., Greil, R., Tausch, C., Hilfrich, J., Kwasny, W., Menzel, C., Samonigg, H., Seifert, M., Gademann, G., Kaufmann, M., and Wolfgang, J. (2005) Switching of postmenopausal women with endocrine-responsive early breast cancer to anastrozole after 2 years' adjuvant tamoxifen: combined results of ABCSG trial 8 and ARNO 95 trial. *Lancet* **366,** 455–462
12. Keating, G. M. (2005) Posaconazole. *Drugs* **65,** 1553–1567
13. Lacroix, C., de Kerviler, E., Morel, P., Derouin, F., and Feuilhade de Chavin, M. (2005) *Madurella mycetomatis* mycetoma treated successfully with oral voriconazole. *Br. J. Dermatol.* **152,** 1067–1068
14. Venkatakrishnan, K., von Moltke, L. L., and Greenblatt, D. J. (2000) Effects of the antifungal agents on oxidative drug metabolism: clinical relevance. *Clin. Pharmacokinet.* **38,** 111–180
15. Ouellet, H., Podust, L. M., and de Montellano, P. R. (2008) *Mycobacterium tuberculosis* CYP130: crystal structure, biophysical characterization, and interactions with antifungal azole drugs. *J. Biol. Chem.* **283,** 5069–5080
16. Ekroos, M., and Sjögren, T. (2006) Structural basis for ligand promiscuity in cytochrome P450 3A4. *Proc. Natl. Acad. Sci. U.S.A.* **103,** 13682–13687
17. Cupp-Vickery, J. R., Garcia, C., Hofacre, A., and McGee-Estrada, K. (2001) Ketoconazole-induced conformational changes in the active site of cytochrome P450eryF. *J. Mol. Biol.* **311,** 101–110
18. Yano, J. K., Koo, L. S., Schuller, D. J., Li, H., Ortiz de Montellano, P. R., and Poulos, T. L. (2000) Crystal structure of a thermophilic cytochrome P450 from the archaeon *Sulfolobus solfataricus*. *J. Biol. Chem.* **275,** 31086–31092
19. Vallurupalli, P., Hansen, D. F., and Kay, L. E. (2008) Structures of invisible, excited protein states by relaxation dispersion NMR spectroscopy. *Proc. Natl. Acad. Sci. U.S.A.* **105,** 11766–11771
20. Serrano, P., Pedrini, B., Geralt, M., Jaudzems, K., Mohanty, B., Horst, R., Herrmann, T., Elsliger, M. A., Wilson, I. A., and Wüthrich, K. (2010) Comparison of NMR and crystal structures highlights conformational isomerism in protein active sites. *Acta Crystallogr. Sect. F Struct. Biol. Cryst. Commun.* **66,** 1393–1405
21. Banci, L., Bertini, I., Eltis, L. D., and Pierattelli, R. (1993) Spectroscopic characterization of a newly isolated cytochrome P450 from *Rhodococcus rhodochrous*. *Biophys. J.* **65,** 806–813
22. Banci, L., Bertini, I., Marconi, S., Pierattelli, R., and Sligar, S. G. (1994) Cytochrome P450 and aromatic bases: A 1H NMR study. *J. Am. Chem. Soc.* **116,** 4866–4873
23. Pochapsky, S. S., Pochapsky, T. C., and Wei, J. W. (2003) A model for effector activity in a highly specific biological electron transfer complex: the cytochrome P450(cam)-putidaredoxin couple. *Biochemistry* **42,** 5649–5656
24. Poulos, T. L., Finzel, B. C., Gunsalus, I. C., Wagner, G. C., and Kraut, J. (1985) The 2.6-A crystal structure of *Pseudomonas putida* cytochrome P-450. *J. Biol. Chem.* **260,** 16122–16130
25. Poulos, T. L., Finzel, B. C., and Howard, A. J. (1986) Crystal structure of substrate-free *Pseudomonas putida* cytochrome P-450. *Biochemistry* **25,** 5314–5322
26. Poulos, T. L., Finzel, B. C., and Howard, A. J. (1987) High-resolution crystal structure of cytochrome P450cam. *J. Mol. Biol.* **195,** 687–700
27. Li, H., and Poulos, T. L. (1997) The structure of the cytochrome p450BM-3 haem domain complexed with the fatty acid substrate, palmitoleic acid. *Nat. Struct. Biol.* **4,** 140–146
28. Raag, R., and Poulos, T. L. (1991) Crystal structures of cytochrome P-450CAM complexed with camphane, thiocamphor, and adamantane: factors controlling P-450 substrate hydroxylation. *Biochemistry* **30,** 2674–2684
29. Vidakovic, M., Sligar, S. G., Li, H., and Poulos, T. L. (1998) Understanding the role of the essential Asp251 in cytochrome p450cam using site-directed mutagenesis, crystallography, and kinetic solvent isotope effect. *Biochemistry* **37,** 9211–9219
30. Estrada, D. F., Skinner, A. L., Laurence, J. S., and Scott, E. E. (2014) Human cytochrome P450 17A1 conformational selection: modulation by ligand and cytochrome $b_5$. *J. Biol. Chem.* **289,** 14310–14320
31. Yamamoto, K., Durr, U. H., Xu, J., Im, S. C., Waskell, L., and Ramamoorthy, A. (2013) Dynamic interaction between membrane-bound full-length cytochrome P450 and cytochrome $b_5$ observed by solid-state NMR spectroscopy. *Sci. Rep.* 2538
32. Ahuja, S., Jahr, N., Im, S. C., Vivekanandan, S., Popovych, N., Le Clair, S. V., Huang, R., Soong, R., Xu, J., Yamamoto, K., Nanga, R. P., Bridges, A., Waskell, L., and Ramamoorthy, A. (2013) A model of the membrane-bound cytochrome $b_5$-cytochrome P450 complex from NMR and mutagenesis data. *J. Biol. Chem.* **288,** 22080–22095
33. Estrada, D. F., Laurence, J. S., and Scott, E. E. (2013) Substrate-modulated cytochrome P450 17A1 and cytochrome $b_5$ interactions revealed by NMR. *J. Biol. Chem.* **288,** 17008–17018
34. Lampe, J. N., Brandman, R., Sivaramakrishnan, S., and de Montellano, P. R. (2010) Two-dimensional NMR and all-atom molecular dynamics of cytochrome P450 CYP119 reveal hidden conformational substrates. *J. Biol. Chem.* **285,** 9594–9603
35. Lampe, J. N., Floor, S. N., Gross, J. D., Nishida, C. R., Jiang, Y., Trnka, M. J., and Ortiz de Montellano, P. R. (2008) Ligand-induced conformational

heterogeneity of cytochrome P450 CYP119 identified by 2D NMR spectroscopy with the unnatural amino acid (13)C-*p*-methoxyphenylalanine. *J. Am. Chem. Soc.* **130,** 16168–16169
36. Roberts, A. G., Díaz, M. D., Lampe, J. N., Shireman, L. M., Grinstead, J. S., Dabrowski, M. J., Pearson, J. T., Bowman, M. K., Atkins, W. M., and Campbell, A. P. (2006) NMR studies of ligand binding to P450eryF provides insight into the mechanism of cooperativity. *Biochemistry* **45,** 1673–1684
37. Jiang, Y., Sivaramakrishnan, S., Hayashi, T., Cohen, S., Moënne-Loccoz, P., Shaik, S., and Ortiz de Montellano, P. R. (2009) Calculated and experimental spin state of seleno cytochrome P450. *Angew. Chem. Int. Ed. Engl.* **48,** 7193–7195
38. Park, S. Y., Yamane, K., Adachi, S., Shiro, Y., Weiss, K. E., and Sligar, S. G. (2000) Crystallization and preliminary x-ray diffraction analysis of a cytochrome P450 (CYP119) from *Sulfolobus solfataricus*. *Acta Crystallogr. D Biol. Crystallogr.* **56,** 1173–1175
39. McLean, M. A., Maves, S. A., Weiss, K. E., Krepich, S., and Sligar, S. G. (1998) Characterization of a cytochrome P450 from the acidothermophilic archaea *Sulfolobus solfataricus*. *Biochem. Biophys. Res. Commun.* **252,** 166–172
40. Kabsch, W. (2010) XDS. *Acta Crystallogr. D Biol. Crystallogr.* **66,** 125–132
41. Winn, M. D., Ballard, C. C., Cowtan, K. D., Dodson, E. J., Emsley, P., Evans, P. R., Keegan, R. M., Krissinel, E. B., Leslie, A. G., McCoy, A., McNicholas, S. J., Murshudov, G. N., Pannu, N. S., Potterton, E. A., Powell, H. R., *et al.* (2011) Overview of the CCP4 suite and current developments. *Acta Crystallogr. D Biol. Crystallogr.* **67,** 235–242
42. Emsley, P., Lohkamp, B., Scott, W. G., and Cowtan, K. (2010) Features and development of Coot. *Acta Crystallogr. D Biol. Crystallogr.* **66,** 486–501
43. Adams, P. D., Afonine, P. V., Bunkóczi, G., Chen, V. B., Davis, I. W., Echols, N., Headd, J. J., Hung, L. W., Kapral, G. J., Grosse-Kunstleve, R. W., McCoy, A. J., Moriarty, N. W., Oeffner, R., Read, R. J., Richardson, D. C., *et al.* (2010) PHENIX: a comprehensive Python-based system for macromolecular structure solution. *Acta Crystallogr. D Biol. Crystallogr.* **66,** 213–221
44. Oliéric, V., Ennifar, E., Meents, A., Fleurant, M., Besnard, C., Pattison, P., Schiltz, M., Schulze-Briese, C., and Dumas, P. (2007) Using x-ray absorption spectra to monitor specific radiation damage to anomalously scattering atoms in macromolecular crystallography. *Acta Crystallogr. D Biol. Crystallogr.* **63,** 759–768
45. Muralidhara, B. K., Negi, S., Chin, C. C., Braun, W., and Halpert, J. R. (2006) Conformational flexibility of mammalian cytochrome P450 2B4 in binding imidazole inhibitors with different ring chemistry and side chains. Solution thermodynamics and molecular modeling. *J. Biol. Chem.* **281,** 8051–8061
46. Koo, L. S., Tschirret-Guth, R. A., Straub, W. E., Moënne-Loccoz, P., Loehr, T. M., and Ortiz de Montellano, P. R. (2000) The active site of the thermophilic CYP119 from *Sulfolobus solfataricus*. *J. Biol. Chem.* **275,** 14112–14123
47. Park, S. Y., Yamane, K., Adachi, S., Shiro, Y., Weiss, K. E., Maves, S. A., and Sligar, S. G. (2002) Thermophilic cytochrome P450 (CYP119) from *Sulfolobus solfataricus*: high resolution structure and functional properties. *J. Inorg. Biochem.* **91,** 491–501
48. Neal, S., Nip, A. M., Zhang, H., and Wishart, D. S. (2003) Rapid and accurate calculation of protein 1H, 13C and 15N chemical shifts. *J. Biomol. NMR* **26,** 215–240
49. Puchkaev, A. V., Koo, L. S., and Ortiz de Montellano, P. R. (2003) Aromatic stacking as a determinant of the thermal stability of CYP119 from *Sulfolobus solfataricus*. *Arch. Biochem. Biophys.* **409,** 52–58
50. Weik, M., and Colletier, J. P. (2010) Temperature-dependent macromolecular X-ray crystallography. *Acta Crystallogr. D Biol. Crystallogr.* **66,** 437–446
51. Fraser, J. S., van den Bedem, H., Samelson, A. J., Lang, P. T., Holton, J. M., Echols, N., and Alber, T. (2011) Accessing protein conformational ensembles using room-temperature x-ray crystallography. *Proc. Natl. Acad. Sci. U.S.A.* **108,** 16247–16252
52. Dunn, A. R., Dmochowski, I. J., Bilwes, A. M., Gray, H. B., and Crane, B. R. (2001) Probing the open state of cytochrome P450cam with ruthenium-linker substrates. *Proc. Natl. Acad. Sci. U.S.A.* **98,** 12420–12425
53. Podust, L. M., Poulos, T. L., and Waterman, M. R. (2001) Crystal structure of cytochrome P450 14α-sterol demethylase (CYP51) from *Mycobacterium tuberculosis* in complex with azole inhibitors. *Proc. Natl. Acad. Sci. U.S.A.* **98,** 3068–3073
54. Scott, E. E., White, M. A., He, Y. A., Johnson, E. F., Stout, C. D., and Halpert, J. R. (2004) Structure of mammalian cytochrome P450 2B4 complexed with 4-(4-chlorophenyl)imidazole at 1.9-A resolution: insight into the range of P450 conformations and the coordination of redox partner binding. *J. Biol. Chem.* **279,** 27294–27301
55. Asciutto, E. K., Young, M. J., Madura, J., Pochapsky, S. S., and Pochapsky, T. C. (2012) Solution structural ensembles of substrate-free cytochrome P450(cam). *Biochemistry* **51,** 3383–3393
56. Stoll, S., Lee, Y. T., Zhang, M., Wilson, R. F., Britt, R. D., and Goodin, D. B. (2012) Double electron-electron resonance shows cytochrome P450cam undergoes a conformational change in solution upon binding substrate. *Proc. Natl. Acad. Sci. U.S.A.* **109,** 12888–12893
57. Mohanty, B., Serrano, P., Pedrini, B., Jaudzems, K., Geralt, M., Horst, R., Herrmann, T., Elsliger, M. A., Wilson, I. A., and Wüthrich, K. (2010) Comparison of NMR and crystal structures for the proteins TM1112 and TM1367. *Acta Crystallogr. Sect. F Struct. Biol. Cryst. Commun.* **66,** 1381–1392
58. Jaudzems, K., Geralt, M., Serrano, P., Mohanty, B., Horst, R., Pedrini, B., Elsliger, M. A., Wilson, I. A., and Wüthrich, K. (2010) NMR structure of the protein NP_247299.1: comparison with the crystal structure. *Acta Crystallogr. Sect. F Struct. Biol. Cryst. Commun.* **66,** 1367–1380
59. Nishida, C. R., and Ortiz de Montellano, P. R. (2005) Thermophilic cytochrome P450 enzymes. *Biochem. Biophys. Res. Commun.* **338,** 437–445
60. Harford-Cross, C. F., Carmichael, A. B., Allan, F. K., England, P. A., Rouch, D. A., and Wong, L. L. (2000) Protein engineering of cytochrome p450(cam) (CYP101) for the oxidation of polycyclic aromatic hydrocarbons. *Protein Eng.* **13,** 121–128
61. Nazor, J., Dannenmann, S., Adjei, R. O., Fordjour, Y. B., Ghampson, I. T., Blanusa, M., Roccatano, D., and Schwaneberg, U. (2008) Laboratory evolution of P450 BM3 for mediated electron transfer yielding an activity-improved and reductase-independent variant. *Protein Eng. Des. Sel.* **21,** 29–35
62. Shah, M. B., Kufareva, I., Pascual, J., Zhang, Q., Stout, C. D., and Halpert, J. R. (2013) A structural snapshot of CYP2B4 in complex with paroxetine provides insights into ligand binding and clusters of conformational states. *J. Pharmacol. Exp. Ther.* **346,** 113–120
63. Lee, Y. T., Glazer, E. C., Wilson, R. F., Stout, C. D., and Goodin, D. B. (2011) Three clusters of conformational states in p450cam reveal a multistep pathway for closing of the substrate access channel. *Biochemistry* **50,** 693–703
64. Brandman, R., Lampe, J. N., Brandman, Y., and de Montellano, P. R. (2011) Active-site residues move independently from the rest of the protein in a 200 ns molecular dynamics simulation of cytochrome P450 CYP119. *Arch. Biochem. Biophys.* **509,** 127–132